A *UBVI* AND *uvbyCa*Hβ ANALYSIS OF THE INTERMEDIATE-AGE OPEN CLUSTER, NGC 5822

GIOVANNI CARRARO[1,4], BARBARA J. ANTHONY-TWAROG[2], EDGARDO COSTA[3], BRYCE J. JONES[2], AND BRUCE A. TWAROG[2]

[1] ESO, Alonso de Cordova 3107, Santiago de Chile, Chile; gcarraro@eso.org
[2] Department of Physics and Astronomy, University of Kansas, Lawrence, KS 66045-7582, USA; bjat@ku.edu, bjj8383@ku.edu, btwarog@ku.edu
[3] Departamento de Astronomía, Universidad de Chile, Casilla 36-D, Santiago, Chile; costa@das.uchile.cl

ABSTRACT

NGC 5822 is a richly populated, moderately nearby, intermediate-age open cluster covering an area larger than the full moon on the sky. A CCD survey of the cluster on the *UBVI* and *uvbyCa*Hβ systems shows that the cluster is superposed upon a heavily reddened field of background stars with $E(B-V) > 0.35$ mag, while the cluster has small and uniform reddening at $E(b-y) = 0.075 \pm 0.008$ mag or $E(B-V) = 0.103 \pm 0.011$ mag, based upon 48 and 61 probable A and F dwarf single-star members, respectively. The errors quoted include both internal photometric precision and external photometric uncertainties. The metallicity derived from 61 probable single F-star members is [Fe/H] = -0.058 ± 0.027 (sem) from m_1 and 0.010 ± 0.020 (sem) from hk, for a weighted average of [Fe/H] = -0.019 ± 0.023, where the errors refer to the internal errors from the photometry alone. With reddening and metallicity fixed, the cluster age and apparent distance modulus are obtained through a comparison to appropriate isochrones in both *VI* and *BV*, producing 0.9 ± 0.1 Gyr and 9.85 ± 0.15, respectively. The giant branch remains dominated by two distinct clumps of stars, though the brighter clump seems a better match to the core-He-burning phase while the fainter clump straddles the first-ascent red giant branch. Four potential new clump members have been identified, equally split between the two groups. Reanalysis of the *UBV* two-color data extending well down the main sequence shows it to be optimally matched by reddening near $E(B-V) = 0.10$ rather than the older value of 0.15, leading to [Fe/H] between -0.16 and 0.00 from the ultraviolet excess of the unevolved dwarfs. The impact of the lower reddening and younger age of the cluster on previous analyses of the cluster is discussed.

Key words: open clusters and associations: general – open clusters and associations: individual (NGC 5822)

Online-only material: machine-readable and VO tables

1. INTRODUCTION

The canonical rationale for the study of star clusters is their value as star systems of homogeneous age, distance, and composition, making them ideal testing grounds for stellar structure and evolution, as well as probes of Galactic evolution. However, the growing evidence from Milky Way globular clusters (Piotto 2009) and Magellanic Cloud open clusters (Rubele et al. 2010; Goudfrooij et al. 2011) casts serious doubt on the degree of temporal and chemical homogeneity for many, if not all, dense, richly populated clusters more than 10^8 years old. Moreover, for nearby clusters the cluster diameter can be comparable in scale to the cluster distance, making isolation of the cluster from the local field star population a challenge in the absence of radial-velocity and/or proper-motion membership a particular problem for the lower-luminosity stars. For more distant clusters, variable reddening and field star contamination can impact the interpretation of observations of a majority of the members of the cluster. Studies of individual clusters therefore are often driven by a specific aspect of stellar or galactic evolution that can best be probed due to the correct combination of cluster parameters and the extent to which they are reliably known, making some clusters iconic examples of a given class, as in M67 and NGC 188 for old open clusters of solar composition and the Hyades for metal-rich clusters of intermediate age.

The focus of this investigation, NGC 5822, is no exception. Some basic properties of the cluster are summarized in Table 1, emphasizing the most recent determinations of metallicity,

reddening, distance, and age from a variety of techniques. With an age of ∼1 Gyr and a metallicity near solar, it exemplifies the properties typical for star clusters of its age within 1 kpc of the Sun (Twarog et al. 1997). In the context of Galactic evolution studies, its role is limited to that of a consistency check for the general cluster population near the Sun. For stellar evolution, however, it falls at or near an age range when important transitions are occurring among the stars dominating the brighter end of the color–magnitude diagram (CMD) and many less populous star clusters are evaporating into the field star background (Janes et al. 1988; Janes & Phelps 1994; Fall 2006; Piskunov et al. 2006; Röser et al. 2010).

For example, stars leaving the NGC 5822 main sequence have masses approaching the range where He ignition switches from quiescent to non-quiescent under degenerate conditions, leading to potentially significant changes in the distribution of stars in the red giant region (Girardi et al. 1998; Girardi 1999). The CMD just below the turnoff is populated by stars with masses where convection first appears as a function of decreasing main-sequence mass, possibly producing the poorly understood Böhm-Vitense gap (Böhm-Vitense & Canterna 1974). Slightly fainter, one expects a fully formed, though potentially deeper, Li-dip than that found in the slightly younger Hyades, but less distorted by post-main-sequence evolution than the equivalent feature seen in slightly older clusters like NGC 3680, NGC 752, and IC 4651 (Pasquini et al. 2004; Anthony-Twarog & Twarog 2004; Anthony-Twarog et al. 2009). The derived cluster age places it on the young side of the Vaughan–Preston gap, but how rapidly the chromospheric activity declines across the gap depends to a significant degree on exactly how young the cluster is (Pace et al. 2009).

---

[4] On leave from Dipartimento di Astronomia, Universitá di Padova, Vicolo Osservatorio 3, I-35122 Padova, Italy.

Table 1
Basic Cluster Information

Source and Method	$E(B-V)$	[Fe/H]	$(m-M)$	Age (Gyr)
Photometry and Moderate-dispersion Spectroscopy					
Stetson (1981)	0.14	...	9.8	...
$uvby$Hβ	DW (21)	...	DW (12)	...
Twarog et al. (1993)	0.15	−0.15	9.85	1.2–2.0
UBV	DW (21), RG (17)	DW (21), RG (13)	MSF	ISO
	0.14	−0.11		
DDO	RG (16)	RG (15)		
Twarog et al. (1997)	0.15	−0.02	10.0	...
		DDO, RG (14)	MSF	...
	...	−0.07	...	...
	...	MDS, RG (3)	...	...
Friel et al. (2002)	0.15	−0.21	...	1.3
	...	MDS (3)	...	MAI
This study	0.10	−0.02	9.85	0.9
$uvbyCa$Hβ	DW (109)	DW (61)	...	...
High-dispersion Spectroscopy					
Luck (1994)	...	0.06	...	...
	...	RG (2)	...	...
Smiljanic et al. (2009)	...	0.04	...	...
	...	RG (5)	...	...
Santos et al. (2009)	...	0.05, 0.12[a] (3)	...	...
	...	RG	...	...
Pace et al. (2010)	0.1	0.05	9.9	1.0
	T-BV,DW	DW (2)	MSF	ISO
	...	0.15	...	...
	...	RG (3)	...	...
Coordinates and Motion					
α, δ (2000)	15:04:24.0	−54:24:05		
l, b	321.5772	+3.5851		
Mermilliod et al. (2008)		$V_{\rm rad} = -29.31 \pm 0.18$ (20)		

Notes. Distance determinations referred to in the table include main-sequence fitting (MSF) and isochrone comparison (ISO). MAI indicated an age determination using morphological age index; T-BV refers to the use of a color–temperature relation for determination of reddening. Methods applied particularly to dwarfs (DW) and giants (RG) are noted. The number of stars included in each analysis is noted in parentheses. Reddening estimates without a method designation are adopted values for the respective analysis.
[a] Different abundances result from the use of two different line lists.

Of primary importance, however, is the combination of a modest distance modulus ($\mu \equiv (m-M) \leqslant 10$) and a rich stellar population. Early CCD (Weller et al. 1991) and photographic work (Twarog et al. 1993) demonstrated that, counting stars within a 15′ radius of the cluster, the CMD is not significantly impacted by field star contamination down to at least two magnitudes below the turnoff, despite its position in the Galactic plane in the general direction of the Galactic center. Moreover, the giant branch and unevolved main sequence are exceptionally rich compared to other nearby clusters of equal or smaller age (Rachford & Canterna 2000). However, in the absence of radial-velocity measures for stars below the turnoff and proper-motion membership estimates for any stars in the field, detailed spectroscopic study of the fainter stars on the unevolved main sequence would be subject to non-negligible contamination by possible background stars, negatively impacting the efficiency of large telescope time devoted to the cluster. With an interest in a comprehensive spectroscopic attack on the cluster members from the giant branch to the unevolved main sequence below solar-mass stars in mind, it was decided that a multi-band photometric survey of the cluster could prove valuable

given the right combination of broadband and intermediate-band filters. As demonstrated by the results of this investigation, *UBVI* CCD photometry meshed with intermediate-band extended Strömgren indices, $uvbyCa$Hβ, allows easy isolation of the cluster members of NGC 5822 from the rich background contamination, while supplying precise estimates of the key cluster parameters of reddening, metallicity, age, and distance.

The outline of the paper is as follows: Section 2 discusses the CCD observations and their reduction to the standard system for both broadband and intermediate-band photometry; Section 3 demonstrates the use of the intermediate-band and narrow-band data to isolate the nearby cluster from the more heavily reddened background stars and to precisely define the cluster metallicity and reddening. Highly probable single cluster members from the field are used in Section 4 to define the cluster age and distance. In Section 5, the adopted members are used to isolate the cluster in a broadband color–color diagram and to rederive the metallicity from the *UBV* photometry of the dwarfs, while Section 6 contains a summary of our conclusions.

Table 2
UBVI Photometric Observations of NGC 5822 and Standard Star Fields

Target	Date	R.A. (2000.0)	Decl. (2000.0)	Filter	Exposures (s)	Air Mass
SA 98	2009 Mar 19	06:52:04.4	−00:19:36	U	2 × 20,2 × 150,2 × 400	1.17–2.35
				B	2 × 20,2 × 100,2 × 200	1.16–2.04
				V	2 × 10,2 × 60,2 × 120	1.15–1.80
				I	2 × 10,2 × 60,2 × 120	1.15–1.92
NGC 5822 (E)	2009 Mar 19	15:04:20.0	−54:23:49	U	30, 200, 2000	1.28–1.30
				B	20, 150, 1500	1.10–1.20
				V	10, 100, 900	1.14–1.15
				I	10, 100, 900	1.10–1.10
PG 1047	2009 Mar 19	10:50:11.3	−00:01:06	U	30, 400	1.46–1.48
				B	20, 200	1.42–1.44
				V	20, 100	1.37–1.38
				I	20, 100	1.40–1.41
NGC 5822 (A)	2010 Mar 11	15:05:29.1	−54:12:44	U	30, 200, 2000	1.08–1.17
				B	20, 150, 1500	1.18–1.20
				V	10, 100, 900	1.21–1.22
				I	10, 100, 900	1.22–1.24
NGC 5822 (B)	2010 Mar 12	15:05:36.3	−54:31:49	U	30, 200, 2000	1.11–1.20
				B	20, 150, 1500	1.20–1.28
				V	10, 100, 900	1.28–1.31
				I	10, 100, 900	1.31–1.33
NGC 5822 (C)	2010 Mar 13	15:03:11.8	−54:33:01	U	30, 200, 2000	1.10–1.30
				B	20, 150, 1500	1.31–1.40
				V	10, 100, 900	1.42–1.45
				I	10, 100, 900	1.45–1.45
NGC 5822 (D)	2010 Mar 14	15:03:11.1	−54:11:59	U	30, 200, 2000	1.06–1.12
				B	20, 150, 1500	1.12–1.19
				V	10, 100, 900	1.21–1.25
				I	10, 100, 900	1.25–1.28

2. OBSERVATIONS AND DATA REDUCTION

2.1. UBVI Photometry

For *UBVI* data, NGC 5822 was observed during two runs; Table 2 provides a log of the *UBVI* observations. During the first run on 2009 March 19, only the central field (E) was observed, while over the second run from 2010 March 11 to 14, an additional four pointings (A, B, C, and D) were observed, leading to an areal coverage 40 arcmin on a side (Figure 1). The observations were carried out with the Y4KCAM camera attached to the Cerro Tololo Inter-American Observatory (CTIO) 1 m telescope, operated by the SMARTS consortium.[5] This camera is equipped with an STA 4064 × 4064 CCD[6] with 15 μm pixels, yielding a scale of 0″.289 pixel^{-1} and a field of view (FOV) of 20′× 20′ at the Cassegrain focus of the CTIO 1 m telescope. The CCD was operated without binning at a nominal gain of 1.44 e^-/ADU, implying a readout noise of 7 e^- per quadrant, with four different amplifiers supplying the simultaneous readout.

All observations were carried out under photometric conditions with seeing below 1″.2. Our *UBVI* instrumental photometric system was defined using standard broadband Kitt Peak *UBVI$_{kc}$* filters.[7] To define the transformation to the standard Johnson–Kron–Cousins system and to correct for atmospheric extinction, standard stars were observed in Landolt fields PG-1047 and SA-98 (Landolt 1992) multiple times at air masses ranging from ∼1.05 to ∼2.4, and covering a color range of $-0.3 \leqslant (B - V) \leqslant 1.7$ mag.

Basic calibration of the CCD frames was done using the Yale/SMARTS y4k reduction script based on the IRAF[8] package CCDRED. For this purpose, bias frames and twilight sky flats were taken every night. Photometry was then performed using the IRAF, DAOPHOT, and PHOTCAL packages. Instrumental magnitudes were extracted following the point-spread function (PSF) method (Stetson 1987). A quadratic, spatially variable, master PSF (PENNY function) was adopted. Aperture corrections were determined using aperture photometry of typically 10–20 bright, isolated stars in the field; corrections were found to vary from 0.160 to 0.290 mag, depending on the filter. The PSF photometry was then aperture-corrected, filter by filter.

After removing problematic stars and stars having only a few observations in the Landolt (1992) catalog, the photometric transformation solutions from 272 measurements per filter were found to be

$$U = u + (3.099 \pm 0.010) + (0.45 \pm 0.01) \times X$$
$$- (0.008 \pm 0.006) \times (U - B)$$
$$B = b + (1.951 \pm 0.012) + (0.27 \pm 0.01) \times X$$
$$- (0.141 \pm 0.007) \times (B - V)$$
$$V = v + (1.892 \pm 0.007) + (0.15 \pm 0.01) \times X$$
$$+ (0.031 \pm 0.007) \times (B - V)$$
$$I = i + (2.696 \pm 0.011) + (0.08 \pm 0.01) \times X$$
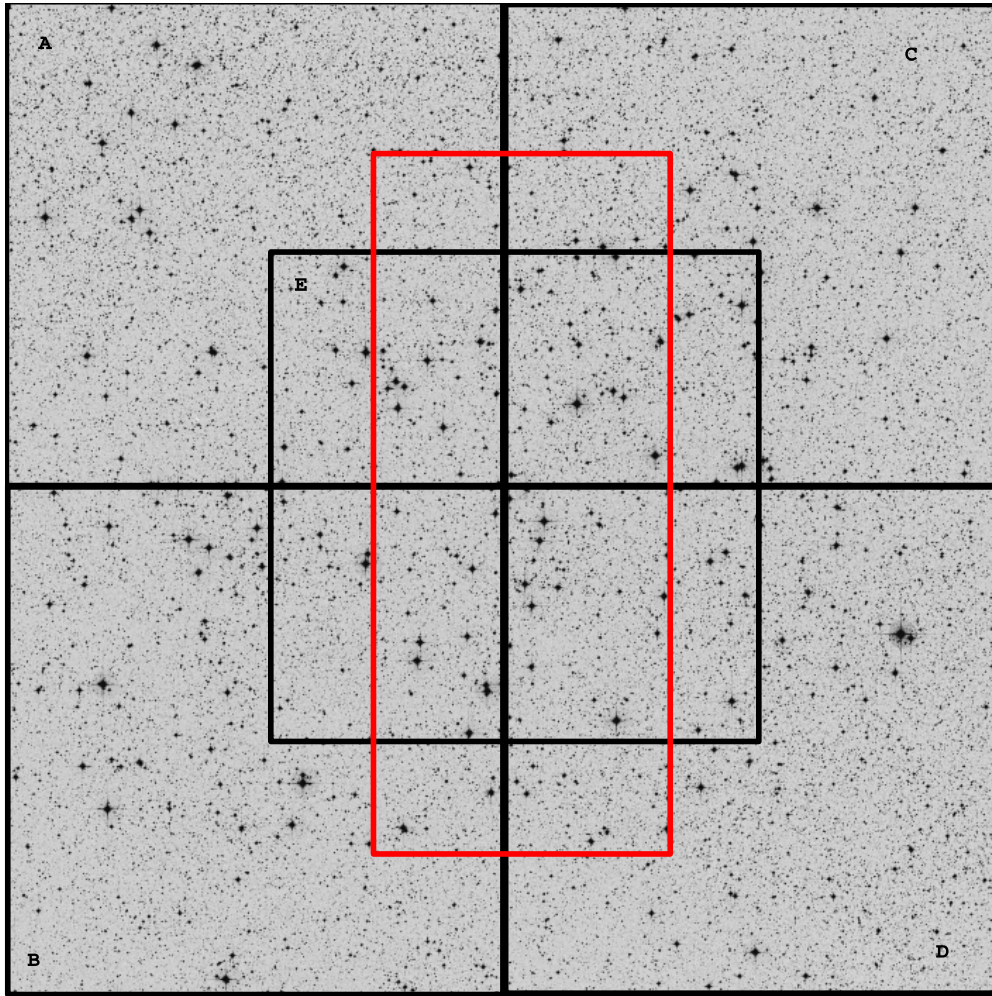$$+ (0.016 \pm 0.008) \times (V - I).$$

Figure 1. Digitized Sky Survey image centered on NGC 5822, illustrating the five Y4KCam pointings. North is up, east to the left, and the field of view is 40 arcmin on a side.

The final rms residuals of the fit to the observations were 0.030, 0.015, 0.010, and 0.010 mag in U, B, V, and I, respectively.

Global photometric errors were estimated using the scheme discussed in Appendix A1 of Patat & Carraro (2001), which takes into account the errors resulting from the PSF fitting procedure within ALLSTAR, and the calibration errors corresponding to the zero point, color term, and extinction errors. In Figure 2 we present our global photometric errors in V, $(B-V)$, $(U-B)$, and $(V-I)$ plotted as a function of V. For clarity, the data have been sorted into an inner region defined by field E (open circles) and an outer region containing all stars not within E (crosses). The bin centers for V have been offset for the outer sample versus the inner region for easier comparison. Quick inspection shows that stars brighter than $V \sim 21$ have average errors in V lower than 0.05 mag, while the average errors remain lower than 0.10 mag in $(B-V)$ for V brighter than 20 and 18.5 in the inner and outer regions, respectively. For $(V-I)$, the average errors remain below 0.10 for V brighter than 21.75 and 21.00, respectively. Predictably higher errors are seen in $(U-B)$, with the error average of 0.1 mag occurring at $V = 18.5$ (inner) and 17.5 (outer), respectively.

2.2. Completeness and Astrometry

Completeness corrections were determined by running artificial star experiments on the data. Basically, several artificial frames were created by adding artificial stars to the original frames. These stars were added at random positions and had the same color and luminosity distribution as the true sample. To avoid generating overcrowding issues, in each experiment artificial stars were added only at a rate up to 20% of the original number of stars. Depending on the frame, this meant that between 1000 and 5000 stars were added. Reprocessing and analysis of the artificial frames leads to the conclusion that the completeness level of our $UBVI$ photometry is better than 90% down to $V = 19.5$.

Our optical catalog was cross-correlated with the Two Micron All Sky Survey (2MASS) and CCD pixel coordinates were converted to R.A. and decl. for J2000.0 equinox, thus providing 2MASS-based astrometry. Our final $UBVI$ photometric catalog for all stars down to $V \sim 21$ mag for any index where the final error is less than ± 0.10 mag is listed in Table 3. Stars are identified through their R.A. and decl. on the 2MASS system.

2.3. Comparison with Previous Photometry

The largest broadband photometric survey of NGC 5822 to date has been that of Twarog et al. (1993), which includes photoelectric data on the UBV system for 144 stars, though not all of the stars have U data. These photoelectric standards were used to calibrate 8 photographic plates each in B and V, leading to precise photographic magnitudes and colors for over 600 stars in an area of $15'$ radius centered on the cluster. Of the 144 photoelectric standards, 135 between $V = 9.49$ and 15.27 were
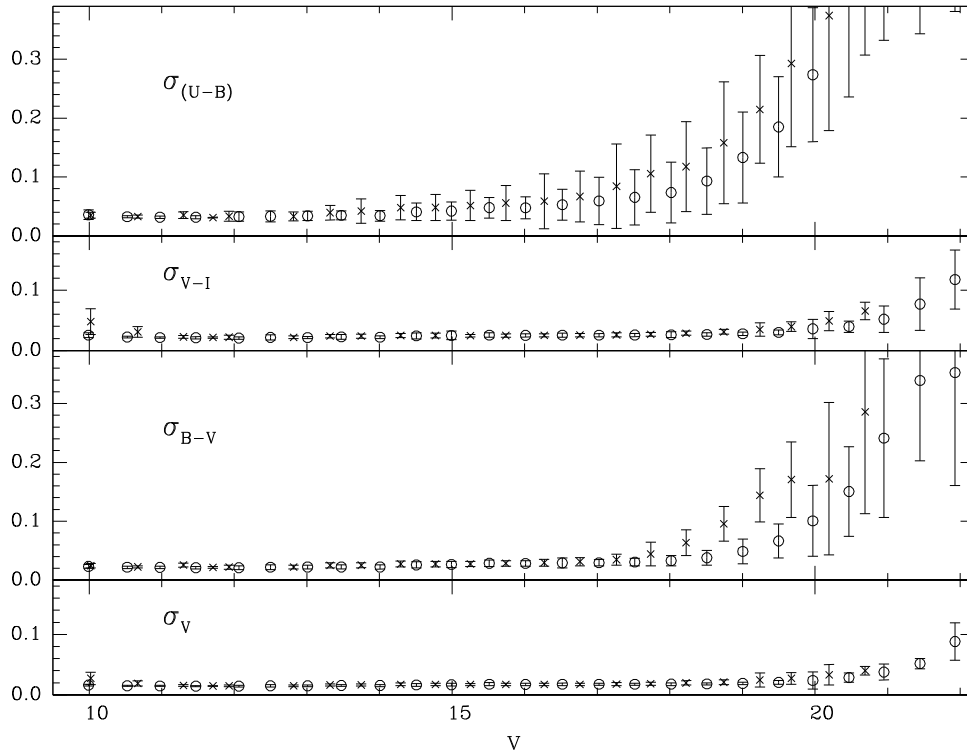
Figure 2. Average photometric errors in V, $(B - V)$, $(U - B)$, and $(V - I)$ as a function of the V magnitude. Open circles refer to stars within region E, while crosses represent data for stars outside of E.

Table 3
Broadband Photometry of Stars in the Field of NGC 5822

$\alpha(2000)$	$\delta(2000)$	V	σ_V	$B - V$	σ_{BV}	$V - I$	σ_{VI}	$U - B$	σ_{UB}
225.9222	−54.3758	9.493	0.018	1.042	0.024	1.053	0.029	0.709	0.034
226.4440	−54.7140	9.513	0.042	1.065	0.024	1.094	0.059	0.624	0.034
226.2494	−54.2987	9.634	0.017	1.215	0.025	1.217	0.032	1.106	0.040
226.1497	−54.5566	9.896	0.019	0.823	0.023	1.125	0.058	0.535	0.033
226.0530	−54.4169	9.942	0.015	0.695	0.022	0.870	0.024	0.486	0.032
226.3524	−54.3832	10.037	0.019	1.649	0.030	1.723	0.027	2.061	0.057
225.9789	−54.5523	10.098	0.017	0.070	0.024	0.084	0.028	−0.083	0.033
226.2603	−54.4403	10.122	0.015	0.095	0.020	0.102	0.021	−0.290	0.031
226.4561	−54.1401	10.159	0.023	1.534	0.030	1.549	0.072	1.229	0.042
226.2061	−54.5067	10.163	0.015	0.410	0.021	0.478	0.021	0.233	0.031
226.5713	−54.5963	10.170	0.019	0.185	0.023	0.163	0.025	0.026	0.032
226.0712	−54.3941	10.202	0.014	0.427	0.020	0.475	0.021	0.302	0.031
225.9583	−54.2418	10.232	0.016	1.020	0.024	1.034	0.026	0.703	0.034
226.6095	−54.1983	10.250	0.025	0.402	0.021	0.406	0.036	0.246	0.032
226.0591	−54.4298	10.281	0.016	1.050	0.024	1.062	0.024	0.771	0.035
226.4627	−54.4184	10.315	0.015	0.216	0.020	0.201	0.022	0.148	0.031
226.5692	−54.2922	10.324	0.028	0.968	0.024	1.023	0.036	0.542	0.033
226.1794	−54.3059	10.338	0.016	1.003	0.024	1.100	0.024	0.608	0.033
226.1643	−54.3512	10.401	0.016	1.040	0.024	1.153	0.023	0.775	0.035
226.6916	−54.2093	10.407	0.017	1.212	0.026	1.244	0.035	1.004	0.038

(This table is available in its entirety in machine-readable and Virtual Observatory (VO) forms in the online journal. A portion is shown here for guidance regarding its form and content.)

found to overlap with the observations in Table 3. The nine stars without matches, i.e., without CCD data, include a number of stars that were too bright to avoid saturation on the CCD images, as well as a few that were probable composites. One star, 114 on the identification system from WEBDA, showed significant residuals in all magnitudes and indices and was dropped from the comparison. The average residuals, in the sense (TAM − Table 3), and their standard deviations are 0.003 ±0.034 and 0.007 ± 0.034 for V and $B − V$, respectively. From 127 stars with UBV data, the analogous residual is −0.015± 0.053 for $U − B$; if the 9 stars with absolute residuals greater than 0.10 mag are excluded, the offset becomes −0.010± 0.038 mag. The trends among the residuals for the various indices as a function of magnitude and color are shown in Figure 3.

A more comprehensive comparison is available through the photographic data which, due to the significant number of plates,
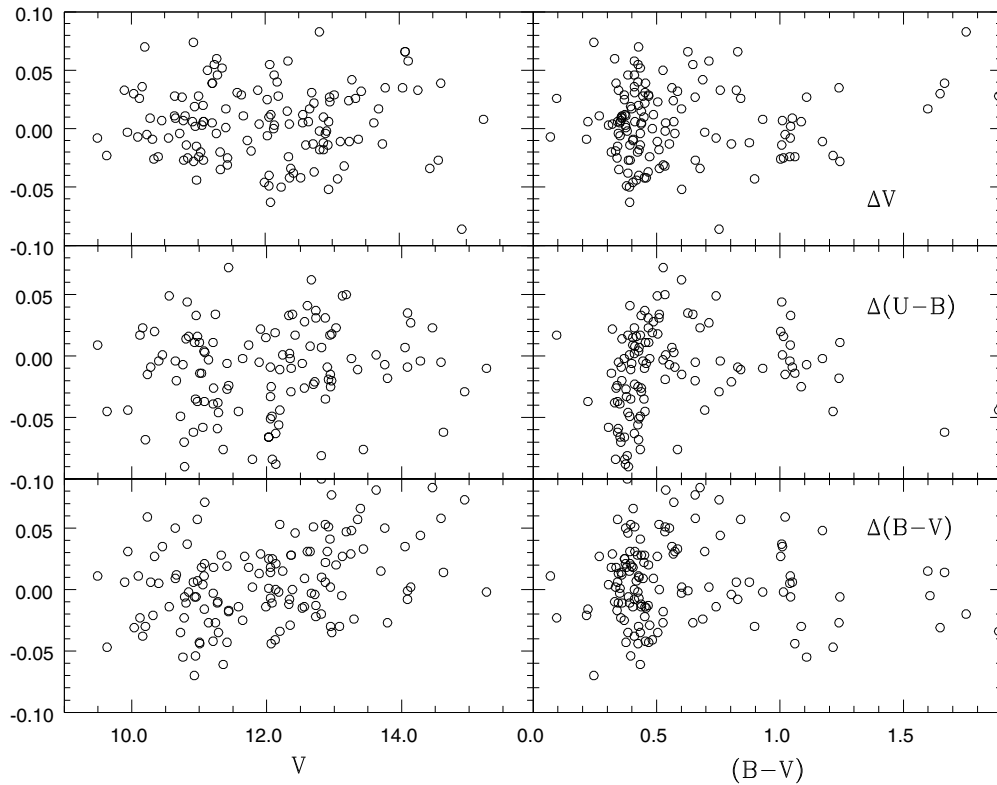
Figure 3. Residuals, in the sense (TAM − Table 3), between the photoelectric and CCD observations for V, $B − V$, and $U − B$ as a function of V and $B − V$.
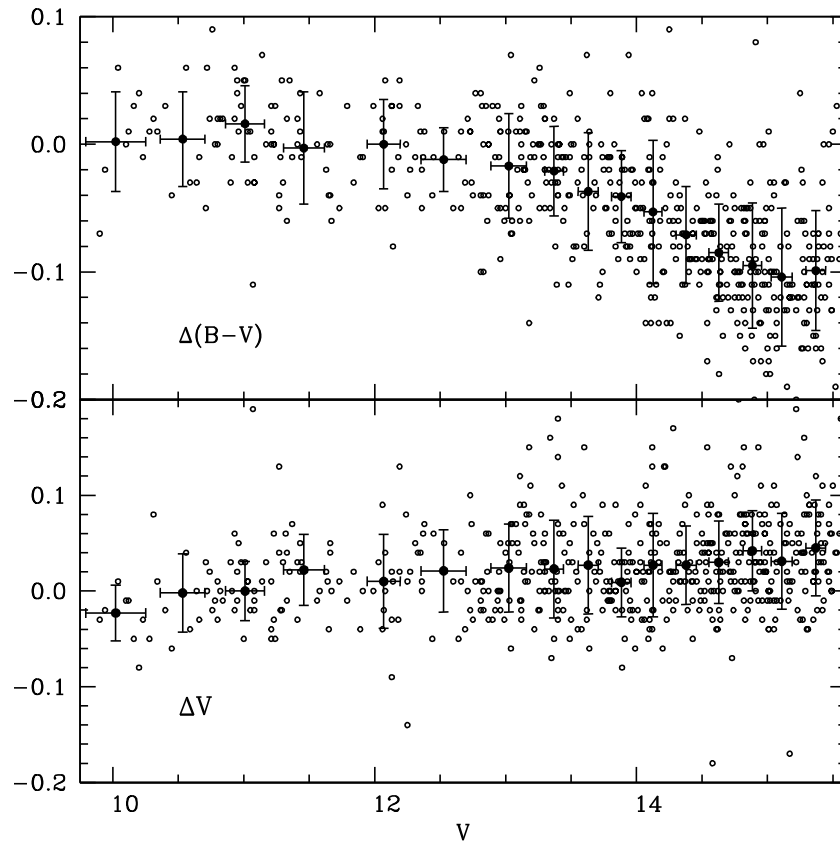

Figure 4. Residuals, in the sense (Table 3 − PG), between the photographic and CCD observations for V and $B − V$ as a function of V. Filled circles represent the average values within a magnitude bin.

has internal precision competitive with the single-measurement photoelectric data within the cluster. The residuals in V and $B − V$, in the sense (Table 3 − PG), as a function of V are illustrated in Figure 4 for 555 stars that overlap with the CCD

sample of Table 3. The mean offset in V is 0.025 ± 0.046 mag, implying that the photographic magnitudes are too bright, with a slight trend of an increasing offset at fainter V. The explanation for this is straightforward in that the photographic data are based upon iris astrophotometer measures which cannot as easily exclude faint companions from the iris measurement as PSF fitting. Thus, stars with faint optical companions will appear brighter in the photographic sample and the impact will be larger for less luminous stars. Support for this explanation comes from the asymmetry in the residuals at a given magnitude, with more scatter on the positive ΔV side, and the fact that the scatter in the residuals for $B - V$ is typically the same or smaller than that for the residuals in V at a given magnitude. Since B and V are calibrated independently, this lack of growth in the scatter for the combined magnitudes can only occur if the errors in B and V are correlated, i.e., the faint companion brightens the magnitude determination in both filters.

The obvious trend in the residuals in $B - V$ can also be attributed to the nature of the photographic calibration, particularly in B. As shown in Figure 3, of 144 photoelectric standards only 9 are fainter than $V = 14$ and only 2 of these fall below $V = 14.75$. Nonlinear terms used in the calibration of the photographic magnitudes to account for the plate response at the faintest magnitudes were very sensitive to these last few standards and modest errors in these standards could easily produce trends of the type illustrated in Figure 4. A similar effect can be seen in a comparable discussion by Nordström et al. (1996) of the similarly processed V photographic data for NGC 3680 (Anthony-Twarog et al. 1991). It should be noted that the probable existence of an offset approaching 0.1 mag in the photographic $B - V$ values near $V = 14.5$ was predicted by Pace et al. (2010) based upon high-dispersion spectroscopic determinations of the temperatures of two solar-type dwarfs.

2.4. uvbyCaHβ Photometry

Intermediate- and narrow-band imaging of NGC 5822 was accomplished over five nights in 2010 June using the CTIO 0.9 m telescope, operated by the SMARTS consortium. The telescope is equipped with a TEK 2048×2048 CCD imager at the $f/13.5$ Cassegrain focus, producing a scale of $0\farcs396$ pixel^{-1} and an FOV of $13\farcm5 \times 13\farcm5$. The images were taken unbinned and read out in QUAD mode at a selected gain of $1.52\ e^-$/ADU. All seven filters were 3×3 inches and came from a set owned jointly by the University of Kansas and Mt. Laguna Observatory.

The cluster was imaged every night, though only four of the five nights were photometric and not every filter was included in every night's observations. Three overlapping fields in the north–south direction were studied, leading to final areal coverage of approximately $13\farcm5 \times 25'$, overlapping nicely with region E of Figure 1. Exposure times in all filters were staggered in length to supply comparable precision from the brightest stars in the field to the unevolved main sequence below $V = 16.5$.

The first four nights of the five-night run were photometric. On two of the photometric nights, a combination of field star and cluster standards was observed to establish transformation equations for V, $(b - y)$, hk, m_1, and c_1; an alternate pair of photometric nights was used to calibrate the first three indices plus Hβ. All standards and program stars were utilized for extinction correction determinations if their observations spanned a suitable range of air mass. A common set of extinction correction coefficients was determined and used for all four photometric nights.

Standard IRAF routines were used to perform initial processing of the frames, i.e., bias subtraction and flat fielding, using dome flats for the y frames and sky flats for the other six filters. A fairly comprehensive discussion of the procedure for obtaining PSF-based instrumental magnitudes and merging multiple frames of a given filter can be found in Anthony-Twarog & Twarog (2000).

Our calibrations to the standard extended Strömgren system are based on aperture photometry in the program cluster, in three open clusters (NGC 6633, NGC 3680, and IC 4651), and of field star standards on each photometric night. For all four photometric nights the seeing was $1\farcs4$–$1\farcs8$, permitting the use of apertures $4\farcs8$ in radius, surrounded by a sky annulus of comparable area. A number of sources were consulted for field star standard values, including the catalog of Twarog & Anthony-Twarog (1995) for V, $b - y$, and hk indices, catalogs of $uvby$Hβ observations by Olsen (1983, 1993, 1994), and compilations of Hβ indices by Hauck & Mermilliod (1998) and Schuster & Nissen (1989). For stars in open clusters, targeted used was made of $uvby$Hβ photoelectric standards in NGC 6633 (Schmidt 1976), red giants in NGC 3680 for which V, $b - y$, and hk photoelectric photometry exists (Anthony-Twarog & Twarog 2004), and $uvby$ photometry of red giants in IC 4651 (Anthony-Twarog & Twarog 2000).

Following standard procedures for Strömgren photometry, a single $(b - y)$ calibration equation was derived for warmer dwarfs and giant stars; too few standards were available for cooler dwarfs to determine an independent calibration for dwarfs with $(b - y) \geqslant 0.42$ so, while the internal precision may be quite good, m_1 and especially c_1 indices for cooler dwarfs may be subject to color-dependent offsets relative to standard relations, a point we will return to in Section 3. Calibrations of m_1 and c_1 for cooler giants are determined independently from calibrations applied to bluer dwarfs. All photoelectric standards, field stars and cluster stars alike, were used to determine slopes and color terms for the calibration equations, as summarized in Table 4. An independent zero point was determined for each calibration equation on each night, based preferentially on field star standards augmented by photoelectric photometry in the three open clusters.

The extension of calibration equations to the merged profile-fit photometry for stars in NGC 5822 is facilitated by determining the average differences between profile-fit indices and indices determined from aperture photometry in the cluster on each photometric night. It was possible to determine the average difference between the aperture and profile-fit indices for 50–90 stars in NGC 5822 with a standard deviation of 0.03 mag or less, so that the "aperture corrections" for each index could be determined to very high precision. In this manner, the calibration equations from each photometric night may be transformed to the aperture photometry in the program cluster, and then by extension to the profile-fit indices in NGC 5822, with an independent zero point for each equation from each photometric night. The precision of the combined zero point applied to the NGC 5822 photometry is also indicated in Table 4. Contributions to this quoted error arise from the standard errors of the mean (sem) from each aperture correction and the sem of the zero point from the calibration equation.

Final photometry on the $uvbyCa$Hβ system can be found in Table 5. For consistency with Table 3, (X, Y) positions are presented as right ascension and declination on the 2MASS system. A plot of the sem for each index as a function of V can be seen in Figure 5. Standard errors of the mean for the indices

Table 4
Characterization of Calibration Equations

	V	$b-y$	$m_1(bd)$	$m_1(rg)$	$c_1(bd)$	$c_1(rg)$	hk	Hβ
Number of photometric nights used	4	4	2	2	2	2	4	2
Calibration equation slope α	1.000	1.025	0.940	1.050	1.020	0.900	1.070	1.170
Color term γ	0.05	. . .	0.11	−0.09	−0.14	0.25	. . .	. . .
Maximum standard deviation for calibration equation for one night	0.022	0.019	0.015	0.031	0.018	0.053	0.034	0.021
Typical contribution to zero point (β) sem from aperture correction	0.002	0.002	0.003	. . .	0.004	. . .	0.003	0.002
Combined sem for final calibration equation	0.004	0.005	0.016	0.020	0.017	0.030	0.007	0.005
Number of photoelectric standards in index calibration	7–17	5–15	3–4	11–14	3–4	11–14	7–17	6–15

Notes. Calibration equations for index x are of the form $x_{\mathrm{std}} = \alpha\, x_{\mathrm{instr}} + \gamma(b-y)_{\mathrm{instr}} + \beta$. Classes of stars include warm dwarfs bd and cool giants rg.

Table 5
$uvbyCa$Hβ Photometry of Stars in the Field of NGC 5822

$\alpha(2000)$	$\delta(2000)$	V	$b-y$	m_1	c_1	hk	Hβ	σ_V	σ_{by}	σ_{m1}	σ_{c1}	σ_{hk}	σ_β	N_y	N_b	N_v	N_u	N_{Ca}	N_n	N_w
226.0096	−54.3398	9.067	0.793	0.505	0.347	1.296	2.562	0.001	0.001	0.002	0.003	0.002	0.002	31	34	25	25	32	25	25
226.1272	−54.5271	9.478	0.843	0.558	0.316	1.433	2.556	0.003	0.004	0.004	0.004	0.004	0.001	15	17	17	17	19	15	15
225.9233	−54.3762	9.510	0.623	0.396	0.355	1.048	2.547	0.002	0.003	0.004	0.004	0.003	0.004	25	24	25	25	28	15	17
226.2482	−54.2994	9.635	0.698	0.487	0.428	1.263	2.547	0.001	0.002	0.003	0.003	0.004	0.004	25	27	25	25	32	24	23
226.1502	−54.5542	9.929	0.615	0.026	0.890	0.371	2.688	0.004	0.005	0.006	0.005	0.006	0.002	18	18	17	17	19	15	15
226.0536	−54.4164	9.950	0.464	0.178	0.774	0.604	2.679	0.001	0.002	0.003	0.003	0.003	0.002	36	37	26	26	35	24	24
225.9813	−54.5503	10.103	0.056	0.072	0.889	0.194	2.842	0.001	0.002	0.002	0.002	0.002	0.003	19	19	17	17	19	15	15
226.2593	−54.4391	10.148	0.058	0.051	0.702	0.163	2.746	0.001	0.001	0.002	0.002	0.002	0.002	35	32	26	26	34	23	24
226.2057	−54.5048	10.184	0.241	0.141	0.911	0.447	2.779	0.004	0.004	0.005	0.004	0.005	0.003	19	19	17	17	19	15	15
225.9581	−54.2437	10.258	0.622	0.375	0.333	0.991	2.559	0.002	0.002	0.003	0.004	0.003	0.001	16	16	16	16	16	16	16
226.0715	−54.3938	10.266	0.244	0.142	0.909	0.449	2.776	0.001	0.002	0.003	0.003	0.002	0.002	33	34	25	25	32	25	25
226.0597	−54.4291	10.292	0.660	0.331	0.454	1.051	2.557	0.002	0.002	0.004	0.004	0.003	0.003	36	37	26	26	35	23	24
226.1785	−54.3066	10.359	0.620	0.270	0.457	0.913	2.556	0.002	0.002	0.003	0.004	0.003	0.003	32	34	25	22	31	25	25
226.1637	−54.3513	10.399	0.646	0.339	0.460	1.060	2.560	0.002	0.002	0.003	0.003	0.002	0.002	33	34	25	25	32	25	25
226.2304	−54.6147	10.426	0.680	0.449	0.411	1.194	2.565	0.001	0.001	0.003	0.007	0.003	0.003	19	19	17	17	15	15	15
226.0719	−54.4719	10.458	0.647	0.300	0.472	1.000	2.567	0.001	0.002	0.002	0.002	0.003	0.002	36	37	26	26	35	21	22
226.1281	−54.5940	10.465	0.649	0.342	0.456	1.049	2.569	0.003	0.003	0.003	0.004	0.003	0.002	19	19	17	17	19	15	15
225.9722	−54.2369	10.616	0.193	0.149	0.954	0.441	2.820	0.001	0.003	0.004	0.003	0.004	0.001	16	16	16	16	16	16	16
225.9115	−54.3010	10.660	0.230	0.177	0.854	0.493	2.759	0.003	0.004	0.005	0.006	0.005	0.010	23	17	21	25	23	15	10
226.1092	−54.5226	10.677	0.306	0.122	0.838	0.433	2.737	0.003	0.004	0.005	0.004	0.005	0.003	19	19	17	17	19	15	15

(This table is available in its entirety in machine-readable and Virtual Observatory (VO) forms in the online journal. A portion is shown here for guidance regarding its form and content.)

are calculated by combining the errors for individual filters in quadrature and are defined solely by the internal, i.e., frame-to-frame, precision of the individual filters. Because of the large number of frames, the sem remain quite small to $V \geqslant 16.5$.

To provide additional validation of our calibration methodology through aperture photometry on photometric nights, we applied identical precepts to observations in NGC 3680 and IC 4651, treating each cluster as a program object. An ex post facto comparison of our calibrated photometry in NGC 3680 to photoelectric V, $b-y$, and hk indices for red giants (Anthony-Twarog & Twarog 2004) demonstrates excellent agreement with the 2004 photometry. Mean differences, in the sense (PE − CCD), for 26 stars for V, $b-y$, and hk are 0.004 ± 0.006, 0.003 ± 0.008, and -0.016 ± 0.015, respectively, where the indicated errors are standard deviations. From 45 dwarfs brighter than $V = 14$, the comparable offsets relative to the 2004 CCD data in NGC 3680, in the sense (2004 − Table 5), are 0.004 ± 0.006, 0.003 ± 0.009, 0.005 ± 0.012, 0.006 ± 0.012, -0.013 ± 0.018, and 0.005 ± 0.007 in V, $b-y$, m_1, c_1, hk, and Hβ, respectively.

Similar comparisons were constructed between calibrated indices for IC 4651 stars to $uvby$ indices for red giants (Anthony-Twarog & Twarog 2004) as well as turnoff and main-sequence stars (Anthony-Twarog & Twarog 1987; Meibom 2000). An additional comparison of Hβ indices was possible with respect to indices from Anthony-Twarog & Twarog (1987). For 14 red giants, the mean differences between indices from Anthony-Twarog & Twarog (1987) and calibrated indices from this run are -0.020 ± 0.037, 0.016 ± 0.021, -0.010 ± 0.031, 0.029 ± 0.032, and -0.001 (one star only) for V, $b-y$, m_1, c_1, and Hβ, respectively. From comparisons with main-sequence and turnoff stars (Anthony-Twarog & Twarog 1987), the average differences are -0.021 ± 0.026, 0.011 ± 0.009, 0.017 ± 0.014, 0.037 ± 0.020, and -0.004 ± 0.012 for the same indices. No Hβ photometry was included in Meibom (2000) and it is likely that the calibration precepts for red giants are substantially different, so the following comparisons, in the sense (MEI − this paper), are derived using 150 main-sequence stars between $V = 11.5$ and 14.0: -0.030 ± 0.013, 0.007 ± 0.027, -0.003 ± 0.027, and 0.040 ± 0.026 for V, $b-y$, m_1, and c_1.
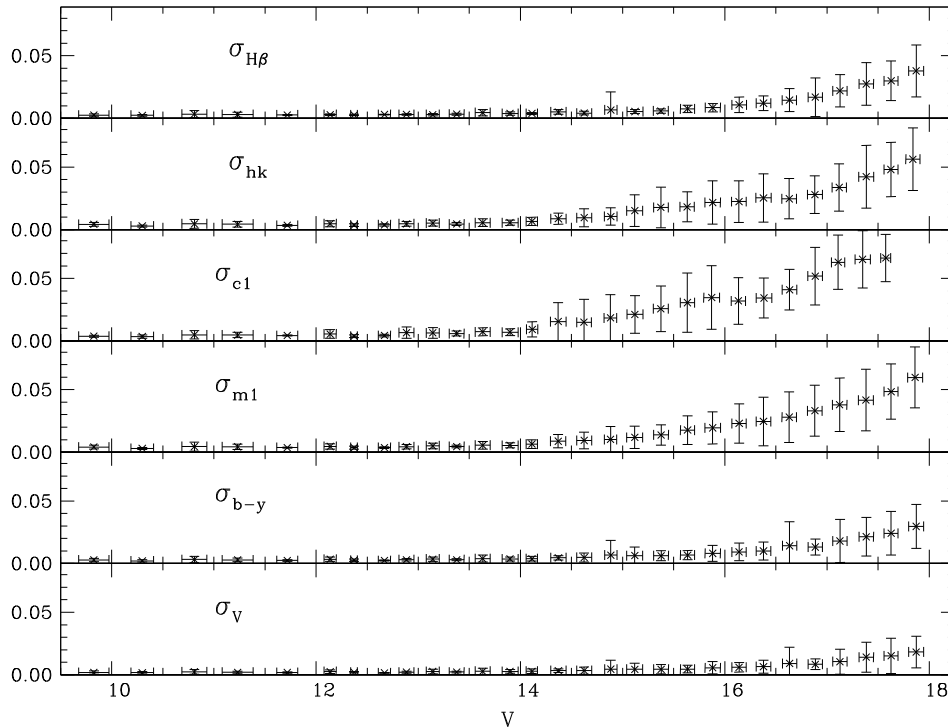
Figure 5. Standard errors of the mean as a function of V for the magnitude and indices of Table 5.
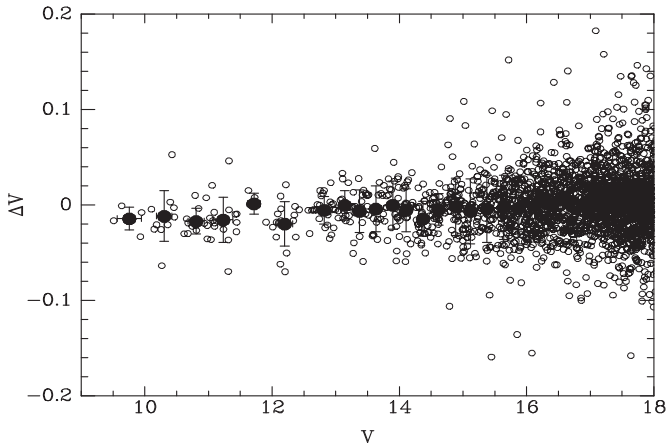

Figure 6. Residuals, in the sense (Table 3 − Table 5), between the V mag as a function of V. Filled circles represent the average values within a magnitude bin.

Figure 7. CMD for all stars within the CCD fields, including all stars in Table 3.

2.5. Comparison to Previous Photometry

On the $uvby$Hβ system, photoelectric data are available for 21 stars from the survey by Stetson (1981). For the 14 stars in common to the two studies, the mean offsets, in the sense (Table 5 − ST), are -0.013 ± 0.011, 0.011 ± 0.025, 0.016 ± 0.040, 0.029 ± 0.043, and 0.000 ± 0.020 for V, $b - y$, m_1, c_1, and Hβ, respectively, where the indicated errors are standard deviations.

On a much larger scale, we can also compare the V system from the y filter with that tied to the traditional broadband V of Table 3. For just under 2250 stars to $V = 18$ that overlap between Tables 3 and 5, the mean offset, in the sense (Table 3 − Table 5), is 0.000 ± 0.033. From Figure 6, where the residuals in V are plotted as a function of V, it should be emphasized that among the 67 stars brighter than $V = 12.5$, the average offset is closer to

-0.015 ± 0.021. The reason for this slight discontinuity remains unknown, but it has no impact on our conclusions.

3. THE CMD AND CLUSTER PARAMETERS: MEMBERSHIP, REDDENING, AND METALLICITY

The traditional CMD based upon $(V, B - V)$ for all stars within the CCD fields is shown in Figure 7. The key structures of the CMD are apparent: a richly populated red giant branch with what appear to be two concentrations of stars with $B - V = 0.96$ to 1.05 at $V = 10.35$ and $B - V = 0.99$ to 1.05 at $V = 10.8$, a well-defined Hertzsprung gap with the turnoff separated from the giant branch in color by an amount typical of clusters with an age of $\sim$1 Gyr, as well as a handful of blue stragglers. The main sequence is richly populated with a sharp blue edge but significant scatter to the red side. The impact of the field star population rises sharply at all colors for V fainter than 13 and grows with increasing V. The role
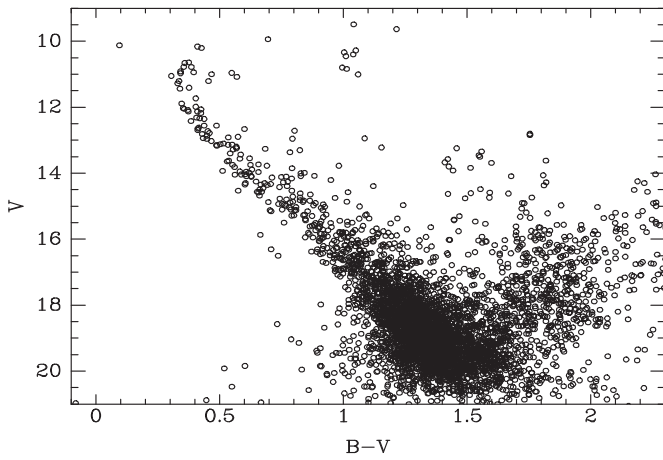
Figure 8. Same as Figure 7 for all stars within a square 13′.5 on a side centered on the cluster.

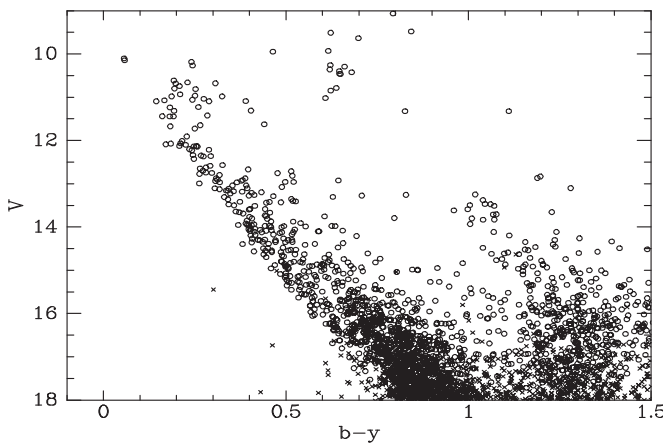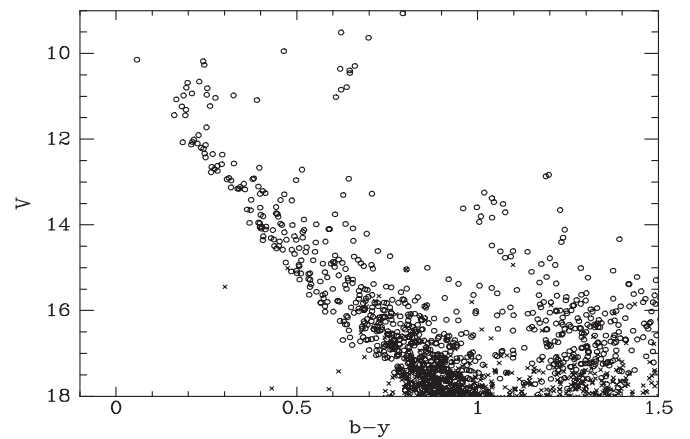**Figure 10.** Same as Figure 9 for stars within a square 13′.5 on a side centered on the cluster.

Figure 9. CMD for all stars in Table 5 with errors in $b - y$ no greater than 0.015 mag (open circles) and no larger than 0.15 mag (crosses).

Figure 11. Two-color trend for stars in Figure 10 with at least two observations each in Hβ wide and narrow and an sem below 0.015 mag in $b - y$ and 0.012 mag for the Hβ index. Filled circles are the 10 giants brighter than $V = 11.05$. The solid line is the mean relation defined by probable cluster members.

of the probable field star contamination in the outer regions of the cluster becomes even more apparent when one restricts the sample to the core region, i.e., stars within a rectangular zone 13′.5 on a side centered on the cluster and chosen to overlap with the central field of the intermediate-band images. This CMD is shown in Figure 8. In addition to the obvious reduction in the number of points, the main-sequence and turnoff region are much better defined with significantly less scatter. Few of the stars with $V \leqslant 13$ are likely to be non-members. Note that part of the improved cluster delineation is a byproduct of the more precise photometry in the cluster core region due to the repeated observations of region E over two observing runs, while stars outside E were observed during only one run. Still, contamination by field stars below $V = 13$ is non-negligible even in the core.

For comparison, we can turn to the $(V, b - y)$ based CMD for all stars in Table 5 brighter than $V = 18$, as shown in Figure 9. Stars with sem errors in $b - y$ below 0.015 are shown as open circles, while stars with errors greater than this cutoff to an sem limit of 0.15 mag are plotted as crosses. Unlike Figure 7, these data come only from a strip 13′.5 by 25′ centered on the cluster core. The turnoff region and giant branch are again richly defined, while contamination by the field sample kicks in for V fainter than 13. The less populated red giant branch makes definitive identification of the two potential clumps at $V = 10.35$ and 10.8 ($b - y = 0.62$–0.68) less obvious. Finally, Figure 10

shows the CMD for the same region as Figure 8. The reduction in field star contamination is apparent, though not as dramatic as the comparison of Figure 7 to Figure 8 due to the smaller differential between the areas.

While restricting our discussion to core stars would reduce the impact of field star contamination on the cluster parameters, it still remains a growing issue for stars fainter than $V = 13$ on the main sequence because this magnitude–color range is occupied by the F dwarfs which are used to define the cluster reddening and metallicity. One can, however, appeal to the reddening and metallicity-independent Hβ indices to enhance the separation between members and non-members. Figure 11 demonstrates the principle. Stars in Figure 10 with at least two observations each in Hβ wide and narrow, an sem below 0.015 mag in $b - y$ and 0.012 mag for the Hβ index, are plotted in Figure 11. Filled circles are the 10 giants brighter than $V = 11.05$. The trend in Figure 11 is gratifyingly obvious. The tight band of stars at the bluest $b - y$ for a given Hβ is defined by cluster members. Moving vertically in the plot, one encounters a large gap of typically 0.25 mag in $b - y$, followed by a wider band of points with the same two-color profile as the cluster members. Since reddening can only move stars vertically in the two-color plot, this implies that the field stars in the CMD are dominated by background stars at a large enough distance that the line-of-sight
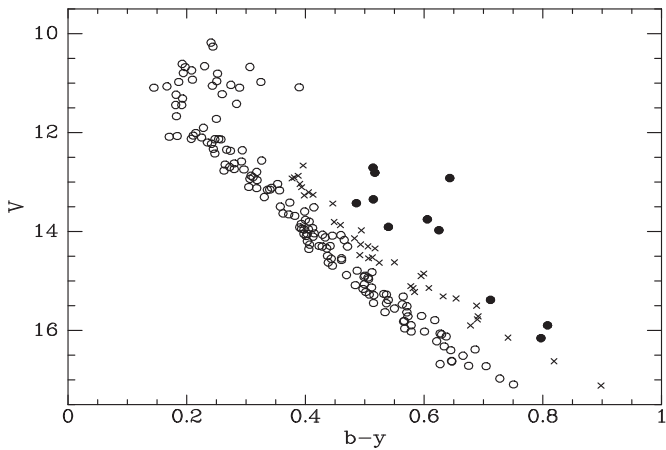
Figure 12. $V, b - y$ CMD for stars in Table 5, excluding giants, that lie within 0.04 mag of the mean relation in Figure 11. Stars must be brighter than $V = 17.5$ with at least two observations each in b, y, β narrow and β wide and have errors in $b - y$ and Hβ below 0.015 mag. Open circles are probable single-star members, crosses are probable binaries, and filled circles are likely foreground non-member dwarfs.

Figure 13. Same as Figure 12 for V, hk.

reddening is at least 0.25 mag larger in $b - y$, or about 0.35 mag larger in $E(B - V)$, than the nearby cluster.

The tight trend defined by the probable members allows us to isolate other likely members from a wider area than the core. A mean relation, shown as a solid line in Figure 11, was derived for the probable cluster stars, excluding the giants, in Figure 11. All stars with $uvby$Hβ photometry, $V \leqslant 17.5$, with at least two observations in b, y, and both β filters, errors in $b - y$ and Hβ below 0.015 mag, and located within 0.04 mag of the solid line in Figure 11, were selected from Table 5. The CMD for these 201 stars is shown in Figure 12. The cluster main-sequence and turnoff region are easily identified while the scatter of stars redward of the cluster CMD is dramatically reduced to stars occupying the predicted region for binaries (crosses) and a handful of stars that are too bright relative to the single-star main sequence to be binary members of the cluster (filled circles). The fact that the latter group falls within the restricted zone around the mean relation in Figure 11 ensures that they must have low reddening similar to the cluster, implying that most must be foreground dwarfs. This can be tested using the LC parameter as derived in Twarog et al. (2007). The LC parameter is based upon a combination of the $b - y$, m_1, and c_1 indices which easily separates cool dwarfs from giants. For the 10 giants in Figure 11, the LC parameter classifies all 10 as evolved stars. By contrast, for the six stars with $(b - y)_0$ greater than 0.5 among the filled circles of Figure 12, the LC indicates that all six are dwarfs.

An additional photometric check on our sample selection is provided in Figure 13 through the (V, hk) CMD. Symbols have the same meaning as in Figure 12. The value of the hk index is its weak sensitivity to reddening but strong sensitivity to temperature changes. Every star that deviates significantly from the mean trend for the cluster (open circles) was identified as a potential binary or non-member in Figure 12, ensuring that at their observed V magnitude, these stars are too red for reasons that cannot be explained through reddening or photometric errors.

Finally, while we have used photometric criteria to identify probable NGC 5822 members (open circles as single stars and crosses as probable binaries in Figures 12 and 13) and non-members (all other stars for which $uvbyCa$Hβ photometry is available), the relative proximity of the cluster might permit us
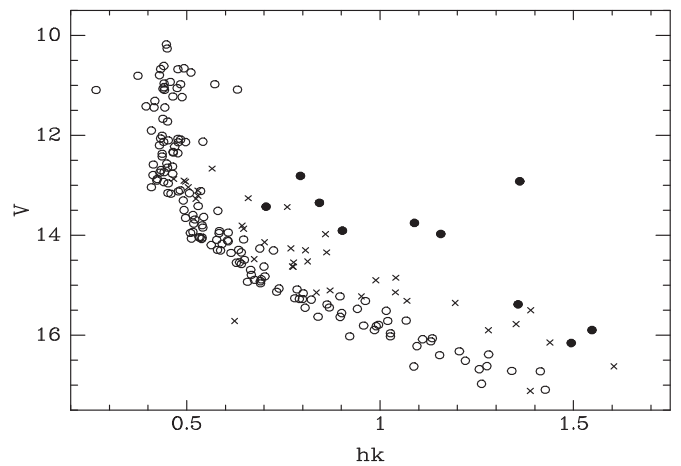
to test the membership results using absolute proper motions from UCAC3 (Zacharias et al. 2000). UCAC3 is a valuable tool for stars down to $R \sim 16.0$, which, in the case of NGC 5822, allows us to probe stars about 5 mag below the turnoff point. A cross-correlation with the UCAC3 database yields 136 probable photometric members and 322 probable photometric non-members.

The resulting vector point diagram is shown in Figure 14, where probable photometric members are indicated by filled symbols and non-members with open symbols. The dashed lines indicate the mean values in the proper-motion components. The mean proper-motion components ($\mu_\alpha \cos(\delta)$, μ_δ) for the non-member sample are -3.98 ± 0.80 and -3.29 ± 0.59 mas yr^{-1}. For the 136 photometric members, the comparable numbers are -7.57 ± 1.45 and -5.32 ± 1.24 mas yr^{-1}.

However, most of the scatter in the mean motion among the smaller sample of photometric members is caused by a handful of exceptional outliers in the proper-motion plot. If the eight most deviant points are excluded, the resulting proper-motion components ($\mu_\alpha \cos(\delta)$ and μ_δ) become -7.90 ± 0.45 and -5.82 ± 0.64 mas yr^{-1}.

The two distributions are different at a significant level, strengthening the case for the photometric classification, though the dispersion in both cases is dominated by the individual errors in the astrometric measures.

With the restricted sample of 153 probable single-star photometric members of NGC 5822 (open circles in Figures 12 and 13), we can now derive the cluster reddening. As in past cluster analyses, use is made of two intrinsic Hβ–$(b - y)_0$ relations to define the intrinsic colors. The first from Olsen (1988) applies to F stars in the Hβ range from 2.58 to 2.72. Additional restrictions on the photometry required at least two observations in every filter used in m_1 and c_1, errors in $b - y$, m_1, c_1, hk, and Hβ less than or equal to 0.015, 0.040, 0.050, 0.050, and 0.015, respectively, and V brighter than 17.5. From 61 F dwarfs that meet all the criteria, the mean $E(b - y)$ is found to be 0.070 ± 0.003 (sem). The second intrinsic color relation is that of Nissen (1988), a slightly modified version of the original relations derived by Crawford (1975, 1979) for F and A stars. For the same 61 F dwarfs, the alternate relation implies $E(b - y) = 0.075 \pm 0.003$ (sem). Because of its age, NGC 5822 has a rich population of A stars. Using the Nissen (1988) relation for the stars with Hβ above 2.72, from 48 stars one finds $E(b - y) = 0.078 \pm 0.002$ (sem). It should be noted that the slightly higher reddening for F stars using the Nissen (1988) relation compared to that of
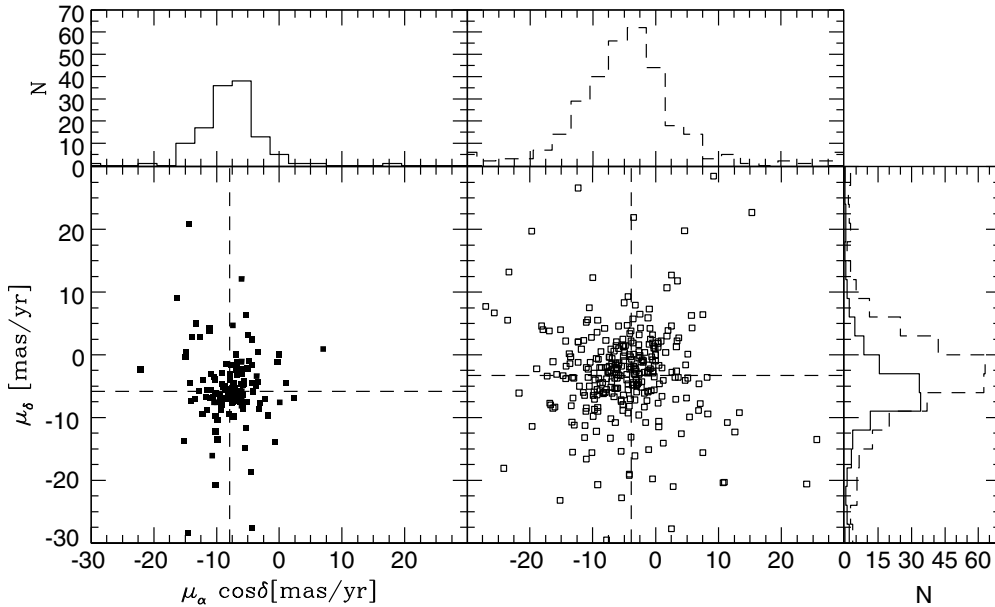
Figure 14. UCAC3 proper-motion distributions for photometrically identified members of NGC 5822 (filled symbols and solid histogram) and non-members (open symbols and dashed histogram). Dashed lines mark the mean motions in each coordinate.

Olsen (1988) is a consistent occurrence from such comparisons (Twarog et al. 2006; Anthony-Twarog et al. 2007). A weighted average of all three results leads to $E(b-y) = 0.075 \pm 0.003$, or $E(B-V) = 0.103 \pm 0.003$ (sem), which we will adopt for the cluster in all future discussions. When combined with the zero-point uncertainties in $b-y$ and Hβ, the total uncertainties in $E(b-y)$ and $E(B-V)$ become ± 0.008 mag and 0.011 mag, respectively.

With the reddening fixed, the next step is the derivation of metallicity, a parameter that can be defined using hk or m_1 coupled to either $b-y$ or Hβ as the primary temperature indicator. In past studies using $uvbyCa$Hβ photometry, the metallicity from hk tied to Hβ invariably has been given the greatest weight due to the greater sensitivity of hk to modest metallicity changes, while the Hβ-based relations allow decoupling between errors in the two indices and minimize the impact of potential reddening variations, if any exist. We will follow the same approach with NGC 5822, allowing us to tie our results directly into the same metallicity scale generated in past intermediate-band cluster studies.

With $E(b-y) = 0.075$, the mean $\delta m_1(\beta)$ for 61 F dwarf probable members between H$\beta = 2.58$ and 2.72 is 0.017 ± 0.003 (sem), where $\delta m_1 = 0.0$ is set at the adopted Hyades metallicity of $+0.12$. On this same scale, NGC 3680 and IC 4651 have $\delta m_1 = +0.027 \pm 0.002$ (sem) (Anthony-Twarog & Twarog 2004) and 0.000 ± 0.002 (sem) (Anthony-Twarog & Twarog 2000), implying that NGC 5822 is clearly lower in [Fe/H] than the Hyades, but not as deficient as NGC 3680. The comparison can be improved because the slope of the δm_1–[Fe/H] relation is color-dependent (Nissen 1988) and the sample of F dwarfs in NGC 5822 is more heavily weighted toward hotter stars than in NGC 3680. For NGC 5822, the δm_1 measure translates to [Fe/H] $= -0.058 \pm 0.027$ (sem), on a scale where NGC 3680 and IC 4651 have [Fe/H] $= -0.175$ and $+0.115$, respectively. As an additional reference point, the photoelectric $uvby$Hβ data of M67 produce [Fe/H] $= -0.06$ (Nissen et al. 1987).

Turning to the hk index, $\delta hk(\beta) = 0.031 \pm 0.006$ (sem), which translates to [Fe/H] $= 0.010 \pm 0.020$ (sem), on a scale

where [Fe/H] $= +0.12$ for the Hyades and NGC 3680 has [Fe/H]$_{hk} = -0.105 \pm 0.016$ (sem). A weighted average of the two metallicity estimates leads to [Fe/H] $= -0.019 \pm 0.023$, where the errors refer to the internal errors from the photometry alone.

As a modest consistency check on our scale, we turn to one of the more recent attempts to redefine the metallicity calibration for the $uvby$ system for dwarfs over a range in temperature from F through K stars. Holmberg et al. (2007, hereafter HNA) discuss the issues with the calibration of Schuster & Nissen (1989), which served as a starting point for the calibrations adopted by Nordström et al. (2004). The net result of the 2004 analysis was a series of metallicity relations covering different color ranges, including a $(b-y)$-based, F-dwarf relation for stars between $b-y = 0.18$ and 0.38, that make direct use of the indices without reference to a standard relation, following the lead of Schuster & Nissen (1989). Equally important for the current discussion is the lack of a c_1 dependence among the terms used in the calibration, a point we will return to below. If we correct the NGC 5822 stars for reddening of $E(b-y) = 0.075$ and apply the relation of Nordström et al. (2004) to 66 F dwarfs, the mean [Fe/H] $= -0.054 \pm 0.031$ (sem) on a scale where the Hyades produces [Fe/H] $= +0.10$.

Since the fainter photometry for the unevolved main sequence of NGC 5822 extends to $(b-y)_0$ redder than 0.38, it could be useful to derive [Fe/H] for the G-dwarfs within the cluster. The problem with this approach is the increasing uncertainty in the c_1 indices at fainter magnitudes and redder colors due to the absence of cooler dwarfs within the calibration from the instrumental to the standard system. Comparison of the dereddened indices to the fiducial c_1–$(b-y)$ relation shows that the difference between the two, in the sense (OBS − FID), starts off positive at the blue end, as expected since the stars in the turnoff region are evolved, then declines to zero near $(b-y)_0 = 0.33$. Redder than this color, the offset should be 0.0 or slightly negative with increasing color. The expected negative δc_1 between the late F and early G stars is a reflection of the increased metallicity sensitivity of c_1 and the declining
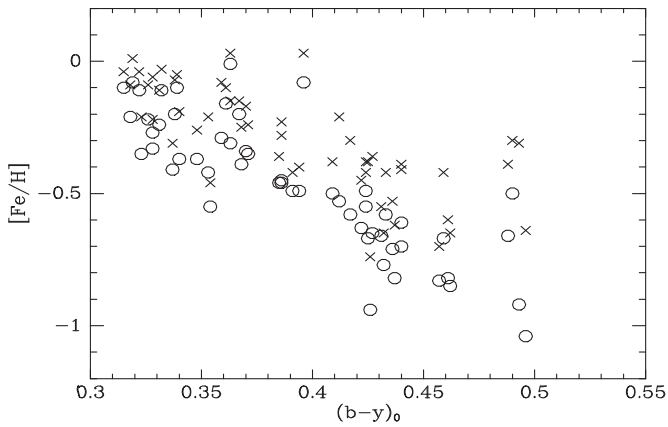
Figure 15. [Fe/H] determined using the revised relations of Casagrande et al. (2011, circles) and the Hβ-based relations of Twarog et al. (2007, crosses).

sensitivity of m_1 at a given $b - y$ (Olsen 1984; Nissen et al. 1987; Twarog et al. 2002, 2007), coupled to the less than Hyades metallicity of NGC 5822. However, at redder $b - y$ the cluster c_1 photometry continues to decline at a faster rate than the fiducial relation, enhancing the negative δc_1 values. For the metallicity determinations discussed above, this trend has no impact because the relations are defined for the hotter stars and have no c_1 dependence. By contrast, for stars redder than $(b - y)_0 = 0.30$, if one adopts an indices-defined relation as found in HNA, where 10 of 20 terms include c_1 in some form, or in Casagrande et al. (2011), where 4 of 11 terms include c_1 in some form, an error in c_1 can have a significant impact on [Fe/H]. The pattern is illustrated in Figure 15 where the newly revised $uvby$ metallicity calibrations for intermediate ($(b-y)_0 < 0.43$) and redder colors ($(b - y)_0 > 0.43$) have been applied to 55 probable members of NGC 5822 (open circles). The mean metallicity from 13 stars with $(b - y)_0 < 0.34$ is -0.21 ± 0.11 (sd), in contrast with [Fe/H] $= -0.06$ from the F-star relation used above and, as one moves redward, the predicted [Fe/H] declines in a linear fashion, reaching a mean near -0.75 at $(b - y)_0$ of 0.50. A virtually identical pattern is produced using the relations in HNA.

As discussed in Twarog et al. (2007), one can reduce the impact of random and systematic photometric errors in c_1 on [Fe/H] if Hβ photometry is available for the cooler dwarfs. The crosses in Figure 15 show the results for the same 55 dwarfs if the Hβ-based metallicity relations derived in Twarog et al. (2007) are applied. The abundance scale adopted in Twarog et al. (2007) is that of Valenti & Fisher (2005). Based upon the revision of the HNA $uvby$ metallicity calibration by Casagrande et al. (2011), which raised the mean [Fe/H] of the HNA scale by ~ 0.1 dex, the two systems in Figure 15 should be similar, if not identical. However, the Hβ-defined abundances for the same 13 stars at the blue end of the sample generate [Fe/H] $= -0.10 \pm 0.09$ (sd) and, while the general trend of declining [Fe/H] with increasing $(b - y)_0$ still applies, the slope is shallower and the scatter at a given $(b - y)_0$ is significantly smaller. From 24 stars redder than $(b - y)_0 = 0.40$, the Casagrande et al. (2011) calibration systematically underestimates [Fe/H] by 0.23 ± 0.11 (sd) dex relative to the Hβ-defined relation.

3.1. Comparison to Previous Results

The reddening and metallicity estimates for NGC 5822 as of 1993 are discussed in detail in Twarog et al. (1993). More recent results are presented in Table 1. For reddening, DDO photometry

of 16 member giants produced $E(B-V) = 0.143 \pm 0.012$ (sem), while the $uvby$Hβ analysis of 21 turnoff stars (Stetson 1987) indicated $E(B - V) = 0.139 \pm 0.009$ (sem). Other analyses produced reddening values ranging between 0.11 and 0.19, but these invariably contained non-members and/or were subject to large uncertainties. The only redetermination of the reddening since then has been that of Pace et al. (2010), obtained by matching the CMD defined by photoelectric measurements to a set of isochrones with the metallicity derived from spectroscopic analysis of two dwarfs. The uncertainty is large, but the result, $E(B - V) = 0.1 \pm 0.05$, is consistent with the value derived in this investigation.

For metallicity, the dominant contributors to the adopted cluster average in Twarog et al. (1993) were DDO photometry ([Fe/H] $= -0.11$) and UBV photometry of the giants and dwarfs ([Fe/H] $= -0.15$). We will rediscuss the UBV-based reddening and metallicity in Section 5. The only spectroscopic results available were the moderate-dispersion spectroscopic analyses of Friel & Janes (1993) for three giants, including two binaries, leading to [Fe/H] $= -0.21$. With the rederivation of the DDO metallicity scale and the rescaling of the moderate-dispersion spectroscopic data of Friel & Janes (1993), Twarog et al. (1997) found [Fe/H] $= -0.03 \pm 0.02$ (sem) from 17 giants. Since the reddening has been lowered to $E(B - V) = 0.10$, some adjustment of this value is required. Fortunately, the impact of lowering the reddening works in opposite directions by raising [Fe/H] from DDO but lowering the spectroscopic estimates. The adjusted value becomes [Fe/H] $= -0.01$ on a scale where NGC 3680, M67, and IC 4651 are -0.10, 0.00, and $+0.10$, respectively.

Until recently, the only high-dispersion spectroscopy of NGC 5822 included three giants, one of which is a definite non-member (Luck 1994). The average [Fe/H] for the two members, including one binary and a potential asymptotic giant branch star, is $+0.06 \pm 0.03$, but the adopted temperature may be ~ 300 K too hot for one of the stars (Smiljanic et al. 2009). If the temperature scale is based purely upon the photometric colors, the mean [Fe/H] is lowered to -0.06. From five giants, Smiljanic et al. (2009) find [Fe/H] $= +0.04 \pm 0.08$ (sd) using spectroscopic temperatures that are, on average, only 37 K cooler than the photometric temperatures derived under the assumption that $E(B - V) = 0.14$. With the adopted lower reddening, the photometric temperatures would be 80 K lower (Houdashelt et al. 2000); an additional drop of 40 K in the adopted temperature scale would lower the spectroscopic abundance by 0.04 dex. Santos et al. (2009) analyze three giants, none of which overlap with the earlier work, and find [Fe/H] $= 0.05 \pm 0.04$ or [Fe/H] $= +0.12 \pm 0.10$, depending upon the adopted line list. Finally, the only dwarfs studied to date are two stars noted earlier in the sample of Pace et al. (2010) which generate [Fe/H] $= +0.05 \pm 0.03$; a rediscussion of the same three giants in Santos et al. (2009) gives [Fe/H] $= 0.15 \pm 0.08$.

4. CLUSTER PROPERTIES—AGE AND DISTANCE

With the reddening and metallicity known, we now turn to the determination of the cluster age and distance through comparison to theoretical isochrones. To optimize the fits, we would prefer to use only single-star members which, with the eventual exception of some key stars among the red giants, restricts the sample to stars with both broadband and intermediate-band photometry, i.e., the central $13'.5 \times 25'$ of the cluster. As detailed in Section 3, we can remove virtually all background stars due to the dramatic increase
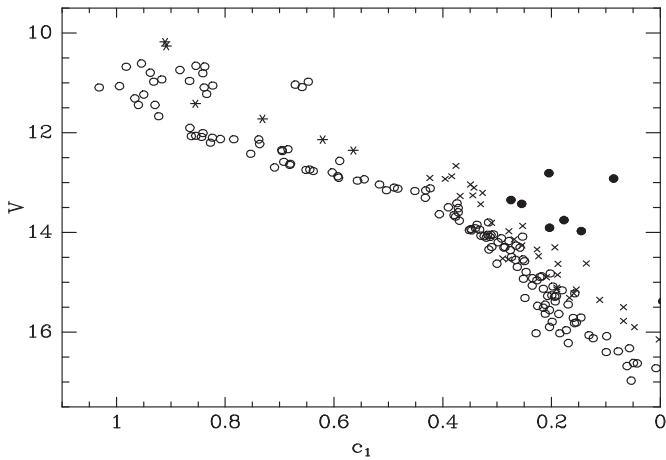
Figure 16. Same as Figure 12 for V, c_1. Starred points are newly identified probable binaries.

Figure 17. $V, V - I$ CMD compared to Y^2 isochrones with [Fe/H] = 0.0, adjusted for $E(V - I) = 0.139$ and $(m - M) = 9.85$. Isochrones have ages of 0.8, 0.9, and 1.0 Gyr. For $V - I < 0.7$, open circles are probable single-star members from photometry. For $V - I > 0.7$, open circles are radial-velocity, single-star members, open triangles are radial-velocity, binary members, starred points are potential photometric members, and crosses are stars with only *UVBI* data.

in reddening beyond the cluster. We can also isolate highly probable foreground stars and cluster binaries with a mass ratio near 1.0 for V fainter than 12.5 by identifying stars that deviate excessively from the mean relations in the $V, b - y$ and V, hk CMDs, as illustrated in Figures 12 and 13. Both approaches become less reliable among hotter stars near the vertical turnoff because binarity among stars in this region shifts the composite system into an area also occupied by evolved single stars. One additional CMD remains which may allow additional composite interlopers to be identified, the (V, c_1) diagram. For unevolved stars, c_1 increases steadily as one moves up the main sequence, with a range of over 0.65 mag from unevolved early G stars to early A stars. Additionally, evolution away from the main sequence causes a correlated increase in c_1 at a given $b - y$ as V becomes brighter. Thus, stars at the vertical turnoff should follow a well-defined trend of larger c_1 at brighter V. Binaries should reveal themselves by being too bright at a given c_1.

Figure 16 shows the (V, c_1) plot for the same stars found in Figures 11 and 12, with symbols having the same meaning. Six additional stars (star symbols) brighter than $V = 12.5$ have been identified as probable binaries because their positions in the CMD are consistent with binarity but incompatible with single stars affected by plausible photometric errors in either V or c_1. Note that the deviant points in this figure at fainter magnitudes have already been identified as such in one of the previous comparisons. In all comparisons of the cluster to theoretical isochrones, any star tagged as deviant as illustrated in Figure 16 will be excluded from the discussion.

For the initial comparison, we use the broadband $(V, V - I)$ CMD, primarily because it has the smallest photometric errors to the faintest magnitude among the *UBVI* indices. The single stars of Figure 16 have been matched to the data of Table 3, generating a sample of 145 stars bluer than $V - I = 0.7$. For the evolved region of the CMD, a list of all stars with $V - I > 0.7$ and V brighter than 12.0 was compiled from Table 3. This list was matched with the radial-velocity results of Mermilliod et al. (1989) and Mermilliod & Mayor (1990), as summarized in Mermilliod et al. (2008). Of the 28 stars included in the radial-velocity study, 20 are found in Table 3; the remaining 8 include 4 non-members and 4 members brighter than $V = 9.75$. The 20 stars for which *VI* data are available include 8 single-star members, 8 binary members, and 4 non-members. The remaining stars redder than 0.7 were matched with the intermediate-band data of Table 5. Three stars were easily
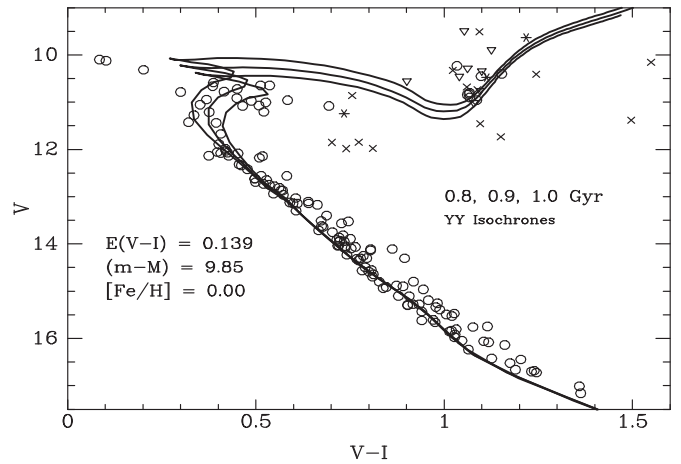
identifiable as heavily reddened background stars, 4 had indices consistent with low reddening, implying cluster members or foreground stars, and 13 were located outside the area covered by the intermediate-band survey. Excluding non-members, the entire sample is plotted in Figure 17. For $V - I$ below 0.7, open circles represent probable single-star members based upon intermediate-band photometry. For $V - I > 0.7$, open circles are single-star, radial-velocity members, open triangles are radial-velocity member binaries, starred points are stars with low reddening implied by intermediate-band photometry, and crosses are stars with only *VI* data.

Superposed are the isochrones with [Fe/H] = 0.00 and ages of 0.8, 0.9, and 1.0 Gyr, shifted by $E(V - I) = 1.35 E(B - V) = 0.139$ and an apparent modulus of $(m - M) = 9.85$. For consistency with the comparable discussions of NGC 3680, NGC 752, and IC 4651 in Anthony-Twarog et al. (2009), the isochrones and interpolation software for specific ages and abundances adopted for the present discussion are those of Y^2 (http://www.astro.yale.edu/demarque/yyiso.html; Yi et al. 2003; Demarque et al. 2004). A modest adjustment of -0.03 mag has been applied to the isochrone M_V scale to make the solar models compatible with our consistently adopted value of $M_V = 4.84$. It should be noted that a shift of this size is larger than the range expected due to the uncertainty in the determination of [Fe/H] (Twarog et al. 2009). No adjustment has been made to the $V - I$ scale. Giving heavy weight to the color of the turnoff, obvious blue stragglers excluded and the uncertainty in the reddening included, the cluster age is well constrained at 0.90 ± 0.10 Gyr.

Moving away from the turnoff region toward the giants, the group of seven stars populating the Hertzsprung gap is likely dominated by foreground field stars rather than stars transitioning to the giant branch given that (1) they lie well below the subgiant branch, (2) this phase is rapid enough that no more than one star should be captured during this transition, and (3) most of these stars lie outside the cluster core region, as expected for a field star distribution. By contrast, despite the lack of four known members in the photometric sample, the giant branch is richly populated, with five new potential members stars falling among the regions dominated by the radial-velocity members. Four of the five new candidates are equally split between the

already discussed dual *clumps* at $V = 10.35$ and 10.8. With the expanded sample and the difference in the color spread among the two clumps, the red giant branch now takes on a more traditional appearance, with the brighter and broader clump at $V = 10.25$–10.45 and $V − I = 1.02$–1.11 potentially associated with core He-burning stars and the fainter, tighter group ($V − I = 1.05$–1.09) populated by first-ascent red giants. In the absence of radial-velocity information clarifying membership and binarity, this interpretation should be regarded with caution. We will return to this point in discussing the second CMD comparison, the (V, $B − V$) diagram.

For the BV CMD analysis, a much larger database exists beyond the photometry of Table 3. As discussed in Section 2, NGC 5822 was observed photoelectrically on a number of occasions prior to the CCD era, with a predominant emphasis on the brightest stars in the field for all studies except Twarog et al. (1993). As the comparisons of Section 2 also demonstrate, the majority of these studies compare favorably with the CCD data in terms of photometric precision. To make optimal use of these data, the photometry of Bruck et al. (1968), Jennens & Helfer (1975), Claria & Lapasset (1985), Claria et al. (1989), and Mermilliod et al. (2008) was adjusted to the photoelectric system of Twarog et al. (1993). The photometry of Table 3 was adjusted by $+0.003$, $+0.007$, and $−0.010$ in V, $B − V$, and $U − B$, respectively, to place it on the photoelectric system. Note that the offsets are so small that adoption of either system for the zero points has a negligible impact on our conclusions. Finally, the high internal precision of the by photometry allows us to readily transfer this data to the BV system with little need to be concerned about distorting the CMD relations. Using only stars classed as single-star cluster members along the main sequence, i.e., excluding stars classed as blue stragglers, subgiants or giants, the ($B − V$) versus ($b − y$) data were fit with two linear relations:

$$(b − y) \leqslant 0.381 \quad B − V = (0.147 \pm 0.011)$$
$$+ (1.015 \pm 0.038) \times (b − y)$$
$$(b − y) > 0.381 \quad B − V = (−0.227 \pm 0.015)$$
$$+ (1.996 \pm 0.030) \times (b − y).$$

The dispersions among the residuals for the transformed photometry are 0.039 and 0.034 mag, respectively. The change in slope near $B − V = 0.53$ is sharp and significant, a point we will return to below.

The individual data sets were assigned a weight based upon their comparison to the adopted photoelectric set and averaged. The stars in Figure 17 were selected and plotted in Figure 18 using the same symbols, reddening, and distance modulus as in Figure 17, adopting the same set of isochrones used, but on the BV system. As with Figure 17, the fit of the isochrones is quite good, though not perfect. The lower main sequence does an excellent job of matching the observations, but the isochrones deviate from the unevolved main sequence at a steeper rate than the cluster stars. At the turnoff, the age of the cluster defined in the region of the red hook is slightly older than that from the VI CMD, but the same within the uncertainties in the colors and the profile of the isochrones at 0.9 ± 0.1 Gyr. As before, all the stars on the subgiant branch at intermediate colors lie well below the predicted location of the isochrone and should be regarded as probable non-members. The exception is the known binary member, which has a luminosity and color indicative of a turnoff–red-giant pair.
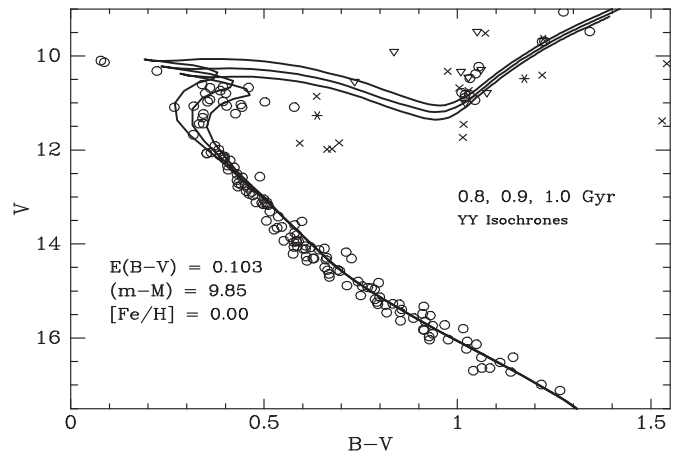

Figure 18. Same as Figure 17 for $E(B − V) = 0.103$ and $(m − M) = 9.85$.

Moving to the red giant branch, the two faintest stars once again lie redward of the predicted isochrone and, while it is tempting to dismiss these stars as non-members, sub-subgiants are known to exist in older open clusters, M67 providing the best examples (Mathieu et al. 2003). If they are members, however, these stars are anomalies, potentially binaries, by definition and tell us nothing about normal red giant evolution. Moving along the more traditional red giant track, the giant branch once again breaks into two distinct regions, with a tight grouping of stars at fainter magnitudes and a broader clump of stars approximately 0.5 mag brighter. The fainter group superposes nicely on the first-ascent red giant branch, while the brighter group scatters systematically to the red. The one probable new member of the red giant clump with both intermediate- and broadband observations falls significantly redward of the giant branch in Figure 18, but its positions in Figures 17 and 9 place this star at the level of the clump on or blueward of the first-ascent giant branch, making it likely that the extreme position in Figure 18 is a product of a modest photometric error.

Are the two groupings in the giant branch simply a separation of stars on the first-ascent and second-ascent giant branches? While post-He-core-ignition tracks are unavailable for the isochrones used in Figures 17 and 18, we can turn to the stellar models of Girardi & Salaris (2001) to evaluate the expected distribution of He-core-burning giants, following the example of Girardi et al. (2000b) using the older models of Girardi et al. (2000a). Figure 19 shows the predicted limiting (faintest) locations for core-He-burning stars as a function of their initial mass (solid line), adjusted for the reddening and distance of NGC 5822; symbols have the same meaning as in Figure 17. Evolved stars of ~ 2.0 solar masses superpose nicely on the fainter clump of stars, but the brighter clump seems to require a spread in mass reaching to ~ 2.5 solar masses. A distribution of 0.6 mag or more in M_V over a narrow range in color among the clump stars is consistent with the synthetic CMDs detailed in Girardi et al. (2000b) for ages from 0.8 to 1.0 Gyr, but no break occurs in the predicted distributions. Assuming the break between the clumps is not simply a statistical fluctuation, the failure of the models to create two distinct clumps, as also claimed for NGC 752 and NGC 7789, has led in part to the suggestion of an extended star formation history within the individual clusters or potentially an indication of the transition to degenerate-He-core ignition among the lowest mass stars on the giant branch. The latter explanation seems unlikely for a cluster as young as NGC 5822. NGC 5822 therefore provides a key
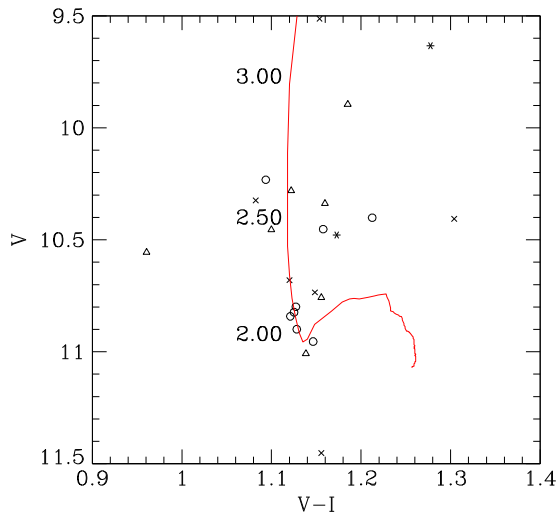
Figure 19. V, $V - I$ CMD of the red giant region compared to core-He-burning models of Girardi & Salaris (2001), adjusted to the distance and reddening of NGC 5822. Initial masses in solar units identify the limiting (faintest) location for evolved stars. Symbols have the same meaning as in Figure 17.
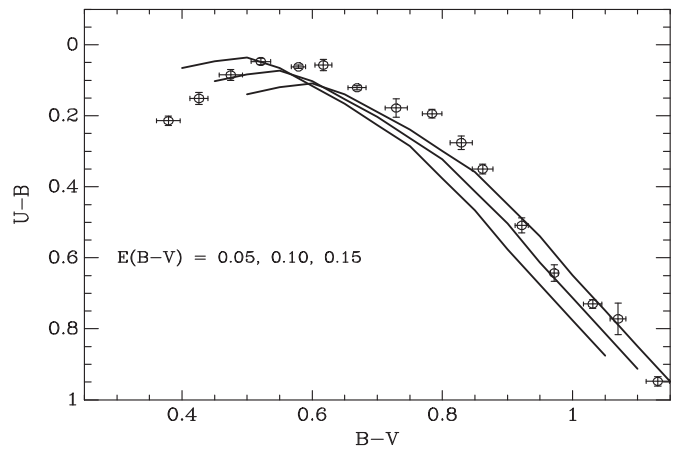

Figure 20. Mean two-color data for probable single-star main-sequence members of NGC 5822 fainter than $V = 12.0$. Error bars in $B - V$ illustrate the dispersion with the binned data, while the error bars in $U - B$ are the standard errors of the mean. Solid lines are the unevolved Hyades relation adjusted for $E(B - V) = 0.05$, 0.10, and 0.15, respectively.

test case at an age where the two observed clumps are equally populated, unlike NGC 7789 and NGC 752 at ages between 1.4 Gyr and 1.8 Gyr, where the fainter clumps are, at best, weakly populated and a challenge to distinguish from first-ascent red giants which should be observable below the clump.

5. REDDENING AND METALLICITY REVISITED: *UBV* PHOTOMETRY

To close the discussion of the cluster properties, we revisit the broadband *UBV* data for the unevolved main-sequence stars of Figure 18. All stars fainter than $V = 12.0$ were sorted in $B - V$ in bins 0.05 mag wide starting at $B - V = 0.35$. The mean values of $U - B$ versus $B - V$ are plotted in Figure 20; error bars represent the dispersion in $B - V$ and the standard error of the mean in $U - B$. Superposed is the standard Hyades two-color relation (Sandage 1969) shifted, from left to right in the plot by $E(B - V) = 0.05$, 0.10, and 0.15. $E(U - B)$ has been derived assuming $E(U - B)/E(B - V) = 0.72 + 0.05 E(B - V)$.

The first feature of the figure requiring comment is the steep slope of the cluster data in contrast with the standard relations for $B - V < 0.55$. The more rapid growth of $U - B$ with declining $B - V$ forces the cluster relation to cross the Hyades relation for $E(B - V)$ below 0.10 and, if the standard relations were extended to bluer colors, probably for even higher reddening values. Since the points between $B - V = 0.6$ and 0.8 all sit above the Hyades relation, independent of the adopted reddening, this transition to super-Hyades metallicity seems unlikely. A more plausible solution is tied to the rather sharp change in the slope of the $(b - y)$–$(B - V)$ relation near $B - V = 0.53$ noted earlier. It has been known for decades that, in addition to the size of the color shift in $U - B$ above the standard relation being a function of $B - V$ for a given change in [Fe/H], the shift is affected by evolution off the main sequence for stars bluer than $B - V = 0.55$ (Eggen & Sandage 1964). The greater the degree of evolution, the redder $U - B$ appears, with the size of the effect dependent upon $B - V$; the increase in $U - B$ for a given change in magnitude grows as $B - V$ shifts from 0.55 to 0.45 and remains relatively constant to $B - V \sim 0.25$ before declining again. Therefore, we conclude that the steep slope in the two-color diagram and the change in slope for the $(b - y)$–$(B - V)$

relation beginning at $B - V = 0.53$ $((B - V)_0 = 0.43)$ reflects the increasing degree of evolution of stars off the main sequence as $B - V$ declines. Stars bluer than $B - V = 0.55$ should not be used to derive the reddening and/or metallicity. This explains why the analysis of Twarog et al. (1993) generated a reddening value $(E(B - V) = 0.15)$ which now appears to be too large. The *UBV* photoelectric photometry is heavily weighted by stars bluer than $B - V = 0.50$ within the turnoff region affected by evolution. To obtain any estimate of an ultraviolet excess that placed the cluster below the metallicity of the Hyades, as required by the few redder dwarfs with photoelectric data, demanded $E(B - V)$ much greater than 0.10 to compensate for the steepened two-color trend for the bluer stars.

At the red end of the scale where evolution effects should be absent, we can place another constraint on the reddening. For $E(B - V) = 0.15$, the cluster data cross the two-color relation for $B - V = 0.9$; all points redder than this boundary sit below the Hyades relation, again in contradiction with the points at intermediate color. To have the redder cluster data lie at a lower metallicity than the Hyades requires than $E(B - V)$ be no greater than 0.12.

Given the three options for reddening in Figure 20, what metallicity is implied by the two-color data? Using only the mean data redder than $B - V = 0.60$, the ultraviolet excesses were calculated for each point and corrected for the color dependence of the ultraviolet excess to transform the mean value to the determination if all data had $(B - V)_0 = 0.6$, i.e., $\delta_{0.6}$. The simple averages for $E(B - V) = 0.05$, 0.10, and 0.15 are 0.113 ± 0.044 (sd), 0.062 ± 0.031 (sd), and 0.018 ± 0.046 (sd), respectively. Note that the growth in the dispersion for values on either side of $E(B - V) = 0.10$ is a reflection of the larger range in $\delta(U - B)$ created by a color shift in the standard relation which has a more significant impact on the redder dwarfs than stars of intermediate color. The minimum in the dispersion for $E(B - V) = 0.10$ is an indicator that the collective trend among the cluster data optimally matches the profile of the standard relation.

A variety of relations have been derived over the years to transform from $\delta_{0.6}$ to [Fe/H] (Wallerstein 1962; Carney 1979; Cameron 1985; Sandage & Fouts 1987). For convenience we make use of one of the more recent discussions (Karatas & Schuster 2006), adopting their final relation tied to 266 dwarfs

and turnoff stars, which should have the greatest applicability to the data in Figure 20. On a scale where the Hyades, with $\delta_{0.6} = 0.0$, would have [Fe/H] $= +0.09$, the three metallicity estimates for NGC 5822 become [Fe/H] $= -0.46$, -0.16, and $+0.03$. If we had adopted the $U - B$ scale of the CCD survey, shifting $U - B$ values by $+0.010$ mag raises the three values to -0.40, -0.11, and $+0.07$, but also places an even tighter constraint on the upper limit for the allowed reddening if we demand that the mean data for the cluster not cross the Hyades relation among the redder dwarfs. We conclude that the expanded and improved UBV data for NGC 5822 require a slightly lower reddening for the cluster than the original analysis by Twarog et al. (1993), with a most probable range between $E(B - V) = 0.10$ and 0.125 and a coupled [Fe/H] between -0.16 and 0.00, taking into account the uncertainties in the $U - B$ zero point and the zero point of the metallicity calibration.

6. SUMMARY

The intermediate-age open cluster, NGC 5822, has been re-evaluated using an extensive broadband survey covering an area $\sim 40'$ on a side, complemented by a precision $uvbyCaH\beta$ study of the core area of the cluster. The latter sample clearly shows that the nearby cluster is superposed upon a background field of significantly higher reddening than the cluster, making identification and isolation of probable cluster members a straightforward exercise. After photometric elimination of probable foreground and/or binary stars, a consistent reddening of $E(b - y) = 0.075 \pm 0.008$ mag or $E(B - V) = 0.103 \pm 0.011$ mag is derived from analysis of 48 A and 61 F dwarfs. With the reddening defined, metallicity estimates from the m_1 and hk indices imply an effectively solar to slightly subsolar metallicity, consistent with the metallicity from DDO photometry of the rich giant population and some high-dispersion spectroscopic analyses, though not all. Despite a lower reddening and slightly higher metallicity than found in the previous CMD analysis using photographic photometry, the cluster retains the same apparent modulus, $(m - M) = 9.85$, but a younger age (0.9 ± 0.1 Gyr) than derived by Twarog et al. (1993), a byproduct of using significantly improved isochrones.

How do the lower age and reddening impact previous analyses based upon inclusion of cluster members with the previous parameters? Two affected studies should be noted. With the removal of probable field stars and binaries from the CMD and a lower reddening, the Böhm-Vitense gap at $B - V = 0.52$ proposed by Rachford & Canterna (2000) now lies directly over the predicted location for the expected Li-dip in NGC 5822 at $(B - V)_0 = 0.41$ (Anthony-Twarog et al. 2009), though the significance of the gap now seems less apparent. It should be noted that the one apparent break in the distribution of stars with V rather than $B - V$ that remains from the photographic study is the decline in probable members between $V = 11.5$ and 12.0. The $(B - V)_0$ color of this break for a less evolved cluster would place the decline in the $0.20–0.25$ range, more consistent with the original color location of the gap as defined by Böhm-Vitense & Canterna (1974).

A more direct impact of the younger age is a partial alleviation of the need for a dramatic transition from chromospherically active to inactive solar-type stars near the age of 1.3 ± 0.1 Gyr. Pace et al. (2009), using observations of two solar-type stars in NGC 5822, found the stars to be as active as stars of similar mass within the Hyades, Praesepe, and IC 4756, all clusters with ages below 1 Gyr. By contrast, solar-type stars in NGC 3680 and IC 4651 both exhibited low activity levels. With an adopted age of 1.4 Gyr for NGC 3680 and 1.2 Gyr for NGC 5822, they concluded that the physical process driving the activity underwent a dramatic decline over a period of ~ 0.2 Gyr or less. Using the same isochrone set and photometric approach adopted for NGC 5822, Anthony-Twarog et al. (2009) derived ages of 1.5 Gyr and 1.75 Gyr for IC 4651 and NGC 3680, implying a gap of ~ 0.6 Gyr between the chromospherically active and inactive stars.

Finally, the expanded photometric sample has added a number of potential members to the giant branch, including four stars split evenly between the two distinct clumps that define the red giant distribution in open clusters in this age range. The balanced population of the two clumps is unique among open clusters of this age range and, coupled with the distinct break in V between the two groups, is difficult to explain under any scenario involving normal, single-star evolution of a given age. To decide if the bimodality is a product of an extended red giant clump driven by a range in mass among the stars leaving the main sequence or a failure of standard stellar evolution to predict the correct distribution of stars on the first-ascent versus second-ascent red giant branch requires a means of deciding which phase the two groups represent, beyond the simple criterion of location within the CMD. Given that the stars at the turnoff all lie well blueward of the Li-dip, the one obvious means of potentially distinguishing between the two scenarios is a measure of the Li abundances of the two groups; second-ascent (He-core-burning) red giants should be seriously depleted in Li relative to the first-ascent members, which should exhibit a decline relative to the stars at the turnoff.

REFERENCES

Anthony-Twarog, B. J., Deliyannis, C. P., Twarog, B. A., Croxall, K. V., & Cummings, J. 2009, AJ, 138, 1171
Anthony-Twarog, B. J., & Twarog, B. A. 1987, AJ, 94, 122
Anthony-Twarog, B. J., & Twarog, B. A. 2000, AJ, 119, 2282
Anthony-Twarog, B. J., & Twarog, B. A. 2004, AJ, 127, 1000
Anthony-Twarog, B. J., Twarog, B. A., Heim, E. A., & Caldwell, N. 1991, AJ, 102, 1056
Anthony-Twarog, B. J., Twarog, B. A., & Mayer, L. 2007, AJ, 133, 1585
Böhm-Vitense, E., & Canterna, R. 1974, ApJ, 194, 629
Bruck, M. T., Smyth, M. J., & McLachlan, A. 1968, Publ. R. Obs. Edinburgh, 6, 210
Cameron, L. M. 1985, A&A, 146, 59
Carney, B. 1979, ApJ, 233, 211

Casagrande, L., Schoenrich, R., Asplund, M., et al. 2011, A&A, 530, A138
Claria, J. J., & Lapasset, E. 1985, MNRAS, 214, 229
Claria, J. J., Lapasset, E., & Minniti, D. 1989, A&AS, 78, 363
Crawford, D. L. 1975, AJ, 80, 955
Crawford, D. L. 1979, AJ, 84, 1858
Demarque, P., Woo, J.-H., Kim, Y.-C., & Yi, S. K. 2004, ApJS, 155, 667
Eggen, O. J., & Sandage, A. R. 1964, ApJ, 140, 130
Fall, S. M. 2006, ApJ, 652, 1129
Friel, E. D., & Janes, K. A. 1993, A&A, 267, 75
Friel, E. D., Janes, K. A., Tavarez, M., et al. 2002, AJ, 124, 2693
Girardi, L. 1999, MNRAS, 308, 818
Girardi, L., Bressan, A., Bertelli, G., & Chiosi, C. 2000a, A&AS, 141, 371
Girardi, L., Groenewegen, M. A. T., Weiss, A., & Salaris, M. 1998, MNRAS, 301, 149
Girardi, L., Mermilliod, J.-C., & Carraro, G. 2000b, A&A, 354, 892
Girardi, L., & Salaris, M. 2001, MNRAS, 323, 109
Goudfrooij, P., Puzia, T. H., Kozhurina-Platais, V., & Chandar, R. 2011, ApJ, 737, 3
Hauck, B., & Mermilliod, M. 1998, A&AS, 129, 431
Holmberg, J., Nordström, B., & Andersen, J. 2007, A&A, 475, 519
Houdashelt, M. L., Bell, R. A., & Sweigart, A. V. 2000, AJ, 119, 1448
Janes, K. A., & Phelps, R. L. 1994, AJ, 108, 1773
Janes, K. A., Tilley, C., & Lynga, G. 1988, AJ, 95, 771
Jennens, P. A., & Helfer, H. L. 1975, MNRAS, 172, 681
Karatas, Y., & Schuster, W. J. 2006, MNRAS, 371, 1793
Landolt, A. 1992, AJ, 104, 340
Luck, R. E. 1994, ApJS, 91, 309
Mathieu, R. D., van den Berg, M., Torres, G., et al. 2003, AJ, 125, 246
Meibom, S. 2000, A&A, 361, 929
Mermilliod, J.-C., & Mayor, M. 1990, A&A, 237, 61
Mermilliod, J.-C., Mayor, M., Andersen, J., et al. 1989, A&AS, 79, 11
Mermilliod, J.-C., Mayor, M., & Udry, S. 2008, A&A, 485, 303
Nissen, P. E. 1988, A&A, 199, 146
Nissen, P. E., Twarog, B. A., & Crawford, D. L. 1987, AJ, 93, 634
Nordström, B., Andersen, J., & Andersen, M. I. 1996, A&AS, 118, 407
Nordström, B., Mayor, M., Andersen, J., et al. 2004, A&A, 418, 989
Olsen, E. H. 1983, A&AS, 54, 55
Olsen, E. H. 1984, A&AS, 57, 443
Olsen, E. H. 1988, A&A, 189, 173

Olsen, E. H. 1993, A&AS, 102, 89
Olsen, E. H. 1994, A&AS, 106, 257
Pace, G., Danziger, J., Carraro, G., et al. 2010, A&A, 515, 228
Pace, G., Melendez, J., Pasquini, L., et al. 2009, A&A, 499, 9
Pasquini, L., Randich, S., Zoccali, M., et al. 2004, A&A, 424, 951
Patat, F., & Carraro, G. 2001, MNRAS, 325, 1591
Piotto, G. 2009, in IAU Symp. 258, The Ages of Stars, ed. E. E. Mamajek, D. R. Soderblom, & R. F. G. Wyse (Cambridge: Cambridge Univ. Press), 233
Piskunov, A. E., Kharchenko, N. V., Röser, S., Schilbach, E., & Scholz, R.-D. 2006, A&A, 445, 545
Rachford, B. L., & Canterna, R. 2000, AJ, 119, 1296
Röser, S., Kharchenko, N. V., Piskunov, A. E., et al. 2010, Astron. Nachr., 331, 519
Rubele, S., Kerber, L., & Girardi, L. 2010, MNRAS, 403, 1156
Sandage, A. R. 1969, ApJ, 158, 1115
Sandage, A. R., & Fouts, G. 1987, AJ, 92, 74
Santos, N. C., Lovis, C., Pace, C. G., Melendez, J., & Naef, D. 2009, A&A, 493, 309
Schmidt, E. G. 1976, PASP, 88, 63
Schuster, W. J., & Nissen, P. E. 1989, A&A, 221, 65
Smiljanic, R., Gauderon, R., North, P., et al. 2009, A&A, 502, 267
Stetson, P. B. 1981, AJ, 86, 1500
Stetson, P. B. 1987, PASP, 99, 191
Twarog, B. A., & Anthony-Twarog, B. J. 1995, AJ, 109, 2828
Twarog, B. A., Anthony-Twarog, B. J., & Edgington-Giordano, F. 2009, PASP, 121, 1312
Twarog, B. A., Anthony-Twarog, B. J., & McClure, R. D. 1993, PASP, 105, 78
Twarog, B. A., Anthony-Twarog, B. J., & Tanner, D. 2002, AJ, 123, 2715
Twarog, B. A., Ashman, K. M., & Anthony-Twarog, B. J. 1997, AJ, 114, 2556
Twarog, B. A., Corder, S., & Anthony-Twarog, B. J. 2006, AJ, 132, 209
Twarog, B. A., Vargas, L. C., & Anthony-Twarog, B. J. 2007, AJ, 134, 1777
Valenti, J. A., & Fisher, D. A. 2005, ApJS, 159, 141
Wallerstein, G. 1962, ApJS, 6, 407
Weller, W., Anthony-Twarog, B. J., & Twarog, B. A. 1991, in Precision Photometry: Astrophysics of the Galaxy, ed. A. G. D. Philip, A. R. Upgren, & K. A. Janes (Schenectady, NY: Davis Press), 345
Yi, S., Kim, Y.-C., & Demarque, P. 2003, ApJS, 144, 259
Zacharias, N., Urban, S. E., Zacharias, M. I., et al. 2000, AJ, 120, 2131